UNIVERSIDADE D
COIMBRA

Rogério Santos Duarte

Diagnosis of Stator Faults in a Multiphase PMSM using a Disturbance Observer

Dissertation presented for the degree of Master of Science in Electrical and Computer Engineering, supervised by Dr. Sérgio Manuel Ângelo da Cruz and presented to the Department of Electrical and Computer Engineering of the Faculty of Sciences and Technology of the University of Coimbra

September 2023

1 2  9 0

UNIVERSIDADE D
COIMBRA

Diagnosis of Stator Faults in a Multiphase PMSM using a Disturbance Observer

Jury:

President: Fernando José Teixeira Estêvão Ferreira

Advisor: Sérgio Manuel Ângelo da Cruz

Examiner: Fernando Manuel dos Santos Perdigão

Coimbra, September 2023

Acknowledgments

I am deeply thankful to Professor Sérgio Cruz for his availability, profound knowledge, and above all, his unyielding encouragement. His mentorship has propelled me to strive for continuous improvement and to reach for ever-higher achievements.

While our paths have not crossed in person, I extend my gratitude to Pedro Gonçalves for his significant contributions to this work, spanning from the intricate six-phase PMSM drive to the utilization of the Ansys model.

I also want to thank the "Instituto de Telecomunicações" for providing the necessary resources to carry out this work, as well as the Department of Electrical and Computer Engineering for these 5 years.

I would like to express my heartfelt gratitude to my parents, Rogério and Adilia, for their unwavering love and their continuous sacrifices on my behalf. Their support has been my foundation throughout this journey. Additionally, I extend my appreciation to my brothers, Fabiana, Dário, and Elza, whose guidance has consistently steered me in the right direction.

A special acknowledgment goes to my girlfriend, Mafalda, whose unwavering support has been a constant source of strength throughout this endeavor.

My appreciation extends to my circle of friends and my housemates for their unflagging support.

I also want to extend my thanks to my fellow laboratory colleagues, with whom I have shared countless hours working towards our shared goals.

Abstract

This dissertation presents a comprehensive investigation into the diagnosis of interturn short-circuit faults in a six-phase permanent magnet synchronous machine (PMSM), employing a disturbance observer (DOB) as the main diagnostic tool.

Chapter 1 introduces the context and motivation that led to this work, outlines the objectives, and sets the stage for the subsequent chapters.

Chapter 2 provides an overview of the current state-of-the-art regarding different types of faults in multiphase machines and the corresponding diagnostic methods employed.

Chapter 3 provides the healthy asymmetrical six-phase PMSM mathematical model, and implemented control system. The chapter ends with the presentation of a deadtime compensation algorithm.

Chapter 4 presents the model of a six-phase PMSM with interturn short-circuits and the employed diagnostic methods for fault detection, including the DOB output signal, stator reference voltages, and stator complex power, primarily used for comparative analysis.

Chapter 5 evaluates the robustness of the proposed diagnostic methods, by validating them through finite element analysis using a 2D cosimulation model developed in Ansys software. Subsequently, the effectiveness of the methods was validated through extensive experimental tests with the six-phase PMSM in different operating conditions. The obtained results show that it is possible to detect effectively interturn short-circuit at medium and high speeds. Difficulties arise when trying to diagnose the most incipient fault cases, which is one turn in short-circuit, especially at low/medium rotor speeds. Also, the location of the faulty phase was possible under 7 short-circuited turns at 1200 rpm.

Chapter 6 concludes this work by comparing the effectiveness of the three fault diagnosis methods proposed and investigated for six-phase PMSMs. The advantages and limitations of each method are discussed, providing valuable insights into their diagnostic capabilities. Moreover, this dissertation lays the foundation for future research endeavors in the field of fault diagnosis for multiphase machines, leaving space for several future research topics.

Keywords: Fault diagnosis, PMSM, multiphase machines, stator faults, interturn short-circuits, disturbance observer.

Resumo

Esta dissertação apresenta uma investigação abrangente sobre o diagnóstico de falhas de curtos-circuitos entre espiras numa máquina síncrona de ímanes permanentes (PMSM) de seis fases, utilizando um observador de perturbação (DOB) como principal ferramenta de diagnóstico.

O Capítulo 1 introduz o contexto e a motivação que levaram a este trabalho, delineia os objetivos e prepara o terreno para os capítulos seguintes.

O Capítulo 2 fornece uma visão geral do estado da arte em relação a diferentes tipos de falhas em máquinas de multifásicas, e os métodos de diagnóstico utilizados.

O Capítulo 3 apresenta o modelo matemático de um PMSM de seis fases saudável na configuração assimétrica e o sistema de controlo implementado. O capítulo termina com a apresentação de um algoritmo de compensação do tempo morto dos inversores.

O Capítulo 4 apresenta o modelo de um PMSM de seis fases com curtos-circuitos entre espiras e os métodos de diagnóstico utilizados para deteção de falhas, incluindo o sinal de saída do DOB, as tensões de referência do estator e a potência complexa do estator, principalmente utilizados para efetuar uma análise comparativa.

O Capítulo 5 avalia a robustez dos métodos de diagnóstico propostos, validando-os através de análise de elementos finitos usando um modelo de cosimulação 2D desenvolvido no software Ansys. Posteriormente, a eficácia dos métodos foi estendida através de extensos dados experimentais com o PMSM de seis fases em diferentes condições de operação. Os resultados obtidos mostram que é possível detetar curtos-circuitos entre espiras a médias e altas velocidades. Dificuldades surgem ao tentar diagnosticar casos de falhas mais incipientes como um curto-circuito numa única espira, especialmente a baixas/médias velocidades do rotor. Além disso, foi possível identificar a fase com falha para 7 espiras em curto-circuito a 1200 rpm.

O Capítulo 6 conclui este trabalho, comparando a eficácia dos três métodos de diagnóstico de falhas propostos e investigados para PMSMs de seis fases. São discutidas as vantagens e limitações de cada método, fornecendo revelações valiosas sobre as suas capacidades de diagnóstico. Além disso, esta dissertação estabelece as bases para futuras investigações no campo

do diagnóstico de falhas em máquinas multifásicas, deixando espaço para diversos tópicos de investigação futuros.

Palavras-chave: Diagnóstico de falhas, PMSM, máquinas multifásicas, falhas no estator, curtos-circuitos entre espiras, observador de perturbações.

"You can do anything you set your mind to."

Benjamin Franklin

Contents

List of Symbols

μ	Short-circuit ratio	
ω_e	Electrical rotor angular speed	rad/s
Ω_m	Mechanical rotor angular speed	rad/s
ψ_{PM}	Flux linkage created by the permanent magnets	Wb
$\mathbf{L}_s$	Stator inductance matrix	H
$\mathbf{R}$	Rotation matrix	
$\mathbf{R}_s$	Stator resistance matrix	Ω
$\mathbf{T}_{vsd}$	Vector space decomposition transformation matrix	
V,W	Discrete matrices used in the disturbance exogenous system	
θ_e	Rotor electrical angular position	rad
θ_m	Rotor mechanical angular position	rad
$\underline{d}_{\alpha\beta}^{-f_s}$	Disturbance observer space vector at a frequency of $-f_s$ in the $\alpha\beta$ subspace	V
$\underline{s}_{dq}$	Stator complex apparent power in dq axes	VA
$\underline{u}_{\alpha\beta}^{-f_s}$	Stator voltage space vector at a frequency of $-f_s$ in the $\alpha\beta$ subspace	V
$d_{\alpha,\beta,x',y'}$	Disturbance observer components in α, β, x', y' axes	V
$d_{d,q,x,y}$	Disturbance observer components in d, q, x, y axes	V
f_s	Fundamental supply frequency	Hz
$i_{a_1 f}$	Current in the faulty winding portion of phase a_1	A
$i_{a_1 h}$	Current in the healthy winding portion of phase a_1	A

i_{sc}	Short-circuit current	A
N_{sc}	Number of short-circuited turns	
N_{tot}	Number of total turns in the winding	
P_s	Rated power	W
p_{dq}	Stator active power in dq axes	W
q_{dq}	Stator reactive power in dq axes	VAr
R_s	Phase resistance	Ω
R_{sc}	Short-circuit resistance	Ω
S_b	Rated complex apparent power	VA
T_d	Deadtime in the power converter	s
t_e	Electromagnetic torque	$\mathrm{N} \cdot \mathrm{m}$
T_s	Sampling period of the control strategy	s
u_s	Stator voltage vector in d, q, x, y subspace	V
u_{sc}	Voltage across the short-circuit	V

List of Acronyms

AO	Adaptative Observer
DOB	Disturbance Observer
DWT	Discrete Wavelet Transform
EKF	Extended Kalman Filter
FCS-MPC	Finite Control Set Model Predictive Control
FFT	Fast Fourier Transform
HHT	Hilbert-Huang Transform
ITSC	Interturn Short-Circuit
KF	Kalman Filter
LO	Luenberger Observer
M-PMSM	Multiphase Permanent Magnet Synchronous Machine
PMSM	Permanent Magnet Synchronous Machine
RCV	Residual Current Vector
SMO	Sliding-Mode Observer
STFT	Short-Time Fourier Transform
WVD	Wigner-Ville Distribution

List of Figures

List of Tables

1 Introduction

1.1 Context and Motivation

Nowadays, we strive to achieve the best performance and efficiency out of every technology. As a consequence, PMSMs have been considered a promising alternative to induction machines in several applications, due to their higher power density and simpler structure. PMSMs are frequently chosen for the power train of electric vehicles or for wind generators [1, 2].

In order to improve even further the performance and efficiency of PMSMs, the idea of using more than the conventional three phases in a machine arose, resulting in the development of multiphase PMSMs (M-PMSMs) [3, 4].

A machine is named multiphase when the number of phases is higher than three ($n > 3$). This category of machines has been gaining attention lately especially in high-power applications. According to [3] multiphase machines provide the following advantages compared to three-phase machines:

- Higher efficiency;
- Lower torque ripple;
- Lower power ratings per phase;
- Capable of fault-tolerant operation against some machine and converter faults;
- Capability to benefit from exclusive modes of operation such as independent control of multi-motor drives supplied from a single converter.

As a consequence of these advantages, M-PMSMs have been gaining interest. The first proposal of a fault tolerant multiphase drive [5] dates back to 1980. In the early 1990s, it was demonstrated the capability of these machines to increase power density by injecting specific current harmonics [6]. This interest, combined with the steady development of digital signal

processors (DSPs), power electronic converters and the newly discovered features lowered the barriers to the industrial market.

M-PMSMs are primarily used in critical systems and applications that prioritize high efficiency and fault-tolerant operation [7]. These applications include ship propulsion [3], traction systems in electric vehicles [1, 8], aircraft systems [9], and systems where availability is crucial, such as offshore wind generation [10, 11].

To further enhance the performance and efficiency of M-PMSMs in critical systems, finite control set model predictive control (FCS-MPC) has gained prominence. FCS-MPC is a control strategy that relies on the discrete model of the system to predict the trajectories of the controlled variables. The increased processing power in the last century made this control strategy viable for multiphase machines which require a high number of operations due to the converters higher number of switching states compared to conventional three-phase machines.

FCS-MPC provides a good transient performance and flexibility to easily define control objectives and constraints in the cost function. However, since the predictions of the controlled variables highly depend on the accuracy of the system model, parameter mismatch or unmodeled dynamics can affect the systems performance.

To address these challenges, a disturbance observer (DOB) can be employed as a control add-on to estimate and compensate the external disturbances and parameter uncertainties. Implementing a DOB can enhance the performance of FCS-MPC by compensating the parameter mismatch or unmodeled dynamics [12]. In the context of a M-PMSM, the DOB may have some specific applications, including:

- Robust Control: Allow the effective operation of the system in the presence of disturbances (deadtime effects, parameter variations, etc).
- Fault Diagnosis: Detect and identify disturbances that may indicate the presence of a fault in the system.
- Power Quality Improvement: Estimate and compensate disturbances (internal or external) that may cause voltage and current harmonics.

The addition of a DOB to FCS-MPC in multiphase machines further enhances their suitability for critical and high-efficiency applications. Considering the critical nature of these applications and the limited information available on fault diagnosis in multiphase machines, the research on fault diagnosis becomes even more crucial.

Interturn short-circuit faults are among the most common faults in electrical machines. A

single turn-to-turn short-circuit quickly propagates to other adjacent turns, eventually culminating into a complete phase-to-phase fault, leading to machine irreversible damage [13].

The study of fault detection becomes crucial as multiphase machines are increasingly implemented in high-cost, critical, and high-performance systems. It serves not only to prevent further damage but also to capitalize on the fault-tolerant operation capabilities of these machines [11]. Early diagnosis plays a pivotal role in this regard, as it enables the modification of the controller operation to allow the machine to continue operating without or with reduced load in the damaged phase, thereby preventing the spread of the short-circuit fault. In practical terms, the most common procedure involves disabling the affected three-phase winding and continuing machine operation with reduced power [11]. Moreover, the concentrated winding configurations in multiphase machines contribute to reduced machine repair costs, making it more feasible to replace the damaged phase, especially in systems where complete machine substitution entails high costs.

Despite the limited research on fault diagnosis in multiphase machines, the use of DOBs in FCS-MPC strategies shows promising results in mitigating errors and improving the system performance. Although implementations are currently scarce, especially in multiphase drives, they are expected to become mainstream control design tools in the future. The increasing amount of applications of multiphase machines in our daily lives and the potential use of DOBs for fault diagnosis, motivates their detailed study.

1.2 Objectives

In the context of the aforementioned motivation, the objectives of this dissertation are to investigate and diagnose stator short-circuit faults in a six-phase PMSM using the output signal of a disturbance observer, and also compare these results with the stator reference voltages, and the stator complex power. To accomplish these objectives, a cosimulation model developed in Ansys software was employed. This model is purpose-built to simulate various stator short-circuit faults, which are subsequently validated through experiments on an assembled system.

By achieving these objectives, this study aims to contribute to the understanding of fault diagnosis in multiphase machines, specifically in the context of stator short-circuit faults in a six-phase PMSM.

2 State-of-the-Art on Fault Diagnosis

This section provides an overview of the current state-of-the-art on the different types of faults, and corresponding diagnostic methods, focusing mainly in interturn short-circuits in multiphase machines.

2.1 Types of Machine Faults

Electric machines such as PMSMs can experience several types of faults that can affect their performance and reliability. These are common to both three-phase and multiphase machines. To prevent further damage and take advantage of the M-PMSM fault-tolerant capabilities, it is important to develop studies on fault diagnosis. The diagram presented in Figure 2.1 exhibits the different types of faults that can occur in PMSM drives [14, 15].

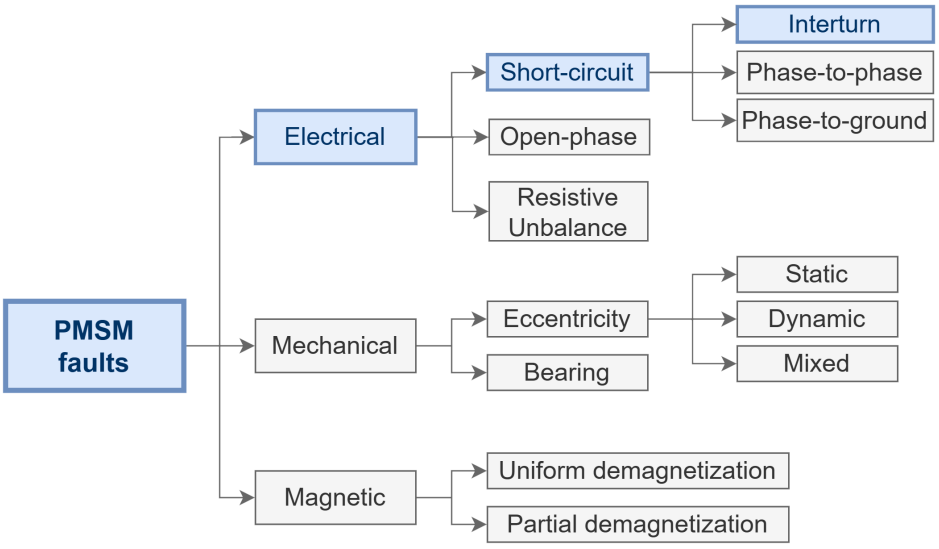

Figure 2.1: Fault classification in a PMSM. Adapted from [15].

The PMSM faults can be divided into three groups: electrical, magnetic, and mechanical.

Electric Faults

The electrical type, involves faults such as **interturn short-circuits** [13, 16, 17], **open phase** [18, 19], and **high resistance connections** [19].

The main focus of this works is the stator interturn short-circuit faults. The progressive degradation of the stator windings insulation is the main cause of short-circuits between the turns of the windings [16]. This degradation causes the current to flow across the turns, producing excessive heat, which may lead to further insulation degradation. If not quickly isolated, a single turn-to-turn short-circuit quickly evolves into a more severe phase-to-phase or phase-to-neutral short-circuit, destroying machine windings. Moreover, the high current flowing across the turns can lead to other faults like the permanent magnets demagnetization.

Magnetic Faults

Magnetic faults such as the partial **demagnetization of the permanent magnets** may occur for instance due to the overheating caused by high localized magnetic fields due for instance to an interturn short-circuit current [20, 21, 22]. Loss of magnetization can also occur due to magnet cracking caused by mechanical stresses. Magnet fading occurs when the magnetization of the permanent magnets in the PMSM decreases over time due to aging or exposure to certain environmental conditions such as overtemperatures leading to a reduction in the torque production and efficiency of the machine [22, 23].

Mechanical Faults

Mechanical faults involve the **bearings of the machine** [24], **eccentricity** [24, 25], **misalignment** and **imbalances**. According to [14], they represent nearly 41% of all low voltage machine faults. Bearing faults result from excessive loads, inadequate lubrication, or material fatigue [26]. Eccentricity is the condition of unequal airgap that exists between the stator and rotor, leading to increased vibration levels [24]. There are two types of eccentricity: static and dynamic eccentricity. Misalignment arises when machine components are not properly aligned, causing additional stress on the bearings of the machine. Imbalances, characterized by uneven distribution of mass within the rotor, generate forces that can lead to the deterioration of the bearings and structural damage over time.

2.2 Diagnostic Methods

In order to avoid catastrophic failures, it is important to develop adequate fault diagnostic techniques, able to detect faults at an early stage of development.

The fault diagnosis task consists in the detection and identification of the fault type as well as its severity and location, all in a short period of time.

The diagnostic techniques can be classified into three different groups [14]:

- Signal-Based
- Artificial Intelligence-Based
- Model-Based

Each one of these categories of diagnostic techniques has its advantages and downsides, which will be briefly pointed out in the following paragraphs.

2.2.1 Signal-Based Methods

Signal-based diagnostic methods are the most common diagnostic methods [14]. It all starts with the machine data acquisition, usually current signals, followed by a feature extraction process which consists in manipulating the acquired signals in different ways. The fault diagnosis is carried out by checking the consistency between the known healthy signal pattern and the signal measured from the real machine, extracted either by using frequency-domain, or time-frequency signal processing techniques.

2.2.1.1 Time-Domain Methods

Time domain diagnostic methods are not very common. Time-domain methods involve the analysis of signals in the time domain to identify abnormalities or faults. In [27], the authors have integrated the Park vector method using the stator phase current with principal component analysis for real-time condition monitoring of the PMSM stator windings. The findings from their study validate the effectiveness of this approach in detecting interturn short-circuits and in the location of the faulty phase.

2.2.1.2 Frequency-Domain Methods

Very often, the time-domain signals are converted into the frequency-domain by different techniques. Fault diagnosis using fast Fourier transform (FFT) is well established and is widely used as the basic signal processing technique.

When it comes to fault diagnosis using the FFT, the literature is vast and well established. Usually, the FFT is applied to the stator current signals in order to extract the current spectrum. According to [26, 28] in the case of an interturn short-circuit fault, the amplitude of the $3f_s$ component has the most obvious increase. As stated in [17], this analysis is adequate in steady-state conditions, but may not be applied to light load and/or variable load and speed.

Frequency-domain methods using the FFT can also be used to analyze the symmetrical components of the stator phase currents. Figure 2.2 illustrates the symmetrical components for an *abc* system. As explained in [17], the amplitudes of the three-phase currents are identical in healthy three-phase machines. Although both positive and negative sequence components are affected by interturn short-circuit faults, the effects are usually more noticeable in the negative-sequence component, due to the unbalanced phase currents caused by this type of fault.

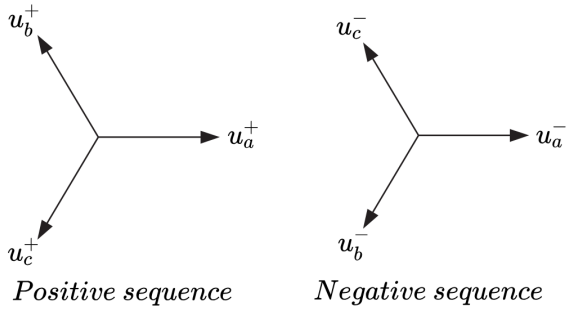

Figure 2.2: Vectorial representation of positive and negative components of an *abc* system.

Despite the many advantages of fault diagnosis using frequency-domain techniques like the FFT, it has several drawbacks such as the long measurement times needed and the requirement of a stationary signal which is impracticable in modern day drives which have high dynamics.

2.2.1.3 Time-Frequency Domain Methods

When operating under nonstationary conditions, time-frequency methods are preferred. These methods involve the decomposition of the signal into time-frequency components, which can provide information about the frequency content and temporal behavior of the signal. The limitations of the frequency methods, such as the need for a stationary signal, lead to the application of time-frequency methods like the short-time Fourier transform (STFT) [14], discrete wavelet transform (DWT) [14], Wigner-Ville distribution (WVD) [29], Hilbert-Huang transform (HHT) [30], among others, in fault diagnosis. Each one of them has its advantages and disadvantages.

The STFT is an improved method based on the FFT that divides the signal into small time windows and then applies the FFT to each one of them. This results in a series of frequency

spectra, one for each time frame, which can then be used to analyze the frequency content of the signal over time, rather than just as a single overall frequency spectrum. The STFT downside is the constant time window width which leads to a trade-off between time and frequency resolution [14, 26].

The DWT is similar to the STFT but has some key differences. The signal can be decomposed into different frequency bands with varying resolutions, allowing for a more detailed analysis of specific frequency ranges. Additionally, the DWT allows the analysis of both time and frequency information simultaneously, which can be useful for certain types of signals such as nonstationary ones [14].

Another time-frequency method is the WVD which is based on the energy distribution of the signal. As stated in [29], WVD possesses a great number of good properties, and it has wide interest for fault detection with nonstationary signal analysis. However, it suffers from cross-terms and is computationally intensive.

The HHT is also well suited for reliable fault detection since it is unaffected by transient conditions which might cause false alarms with other techniques. This technique is based on the empirical mode decomposition that decomposes a signal into a limited number of pure oscilating functions called intrisic mode functions and then applies the Hilbert transform to them [30].

2.2.2 Artificial Intelligence-Based Methods

The most prevalent artificial intelligence (AI) methods employed in fault diagnosis include neural networks [31, 32] and fuzzy logic [33, 34]. These AI techniques typically involve two primary steps: feature extraction and fault classification. In fault diagnosis, neural networks use interconnected nodes to learn and identify patterns in the PMSM data, enabling accurate fault detection, based on the network trained knowledge. Fuzzy logic in PMSM fault diagnosis employs a system that can handle imprecise or uncertain information, allowing for flexible and nuanced fault diagnosis. The AI methods suffer from certain drawbacks, such as the need for substantial amounts of data for effective training, network complexity, and demanding computational resources.

2.2.3 Model-Based Methods

Model-based fault diagnosis techniques use machine models, which may be an analytical model or a finite elements model. An analytical model is a mathematical model of a system which allows to analyze its behaviour. When it comes to PMSM analytical models, the literature is extensive, ranging from simple models to those that take into account faults, or even spatial

harmonics. The analytical model presented in [28], takes into account spatial harmonics. The goal here is trying to bring the analytical model results closer to the experimental ones.

Analytical models are usually written using differential equations, which lead to a state-space representation of the physical object. The state space models are used to design observers and estimators and are applied to a PMSM being used to represent the dynamic behavior of the machine and to identify any faults or abnormalities in its operation. One area of research is the use of observers in combination with control techniques to improve performance as proved in [12] where a M-PMSM disturbance observer was developed, in combination with a predictive current control strategy that reduces unmodelled phenomena such as deadtime effects and spatial harmonics.

The disadvantage of these approaches comes from the fact that the models of the industrial processes or practical systems need to be available.

Another area of application of observers is in the fault detection and diagnosis field. Several methods based on observers and estimators had been proposed in literature. The most common way is by calculating the residuals between the output current that comes from the sensor and the one predicted by the state observer [35].

A model-based strategy for interturn short-circuit fault diagnosis was used in [35]. The fault detection was realized based on a residual current vector (RCV) generated by the difference between the measured current vector and the one estimated by a state observer based on a normal-operation model of the PMSM. To avoid false alarms due to possible undesired perturbations, a decomposition of the RCV signal was made by employing reference frame theory. This way the proposed strategy allowed the correct detection of interturn short-circuit faults and the quantification of its severity.

Many types of observers have been used in literature for fault diagnosis in PMSMs such as the adaptative observer (AO), Luenberger observer (LO), Kalman filter (KF), extended Kalman filter (EKF), and the sliding mode observer (SMO).

Among the methods that use parameter estimation, Kalman filters (KF) are the most common ones. These are a stochastic approach, typically used in observers, and estimators [36] of different PMSM variables such as rotor flux and speed. They are used in sensorless ac drives who have been gaining attention with their advantages such as the lower cost, reduced size of the motor drive set, encoder elimination and increased reliability. They cannot be applied to nonlinear signals which leads to the use of the extended or unscented variants of Kalman filters (EKF and UKF, respectively) that deal with nonlinear signals.

In the past, due to the algorithms complexity compared to Luenberger observers, and the

computational load requirements these techniques were not very widespread. Nowadays with the increasing availability of new low-cost highly elaborate processors, the KFs had been gaining more relevance [36].

A fault tolerant controller, based on observers, robust against sensor faults was proposed for a high performance PMSM in [1]. The position and speed are estimated by a optimal two-stage EKF which reduces computation time, and a back-EMF observer.

It was proposed in [37] a method for interturn short-circuit fault diagnosis based on the estimation of the number of short-circuited turns in a specific faulty PMSG model described in the dq frame due to the EKF algorithm. An indicator of the short-circuit was built from the estimated parameters. This technique allowed accurate fault detection and even the identification of the damaged phase.

In [38], a mathematical model of a faulty PMSG with the interturn short-circuit appearing in the dq frame was developed . The percentage and the location of the fault were detected using the EKF and UKF. It was noticed that the proposed techniques had a robust, fast, and accurate response. On top of that, the results showed that the UKF gave more precise results than the EKF, especially with the increased fault severity. This was due to the UKF not needing linearized equations to approximate the nonlinear model as the EKF does.

As verified, although very popular, the EKF has downsides in some applications compared to other observers such as the UKF and the SMO. A drawback of the EKF is that it linearizes the nonlinear system around the current estimated state, which can lead to large estimation errors if the system is far from the linearization point. On the other hand, SMO does not rely on linearization and can handle a larger class of nonlinear systems. Another disadvantage of the EKF is that it requires the system Jacobian matrices to be continuously differentiable, which can be restrictive for some systems. The SMO does not have this requirement and can handle systems with discontinuous dynamics. Additionally, the EKF has poor performance when dealing with measurement noise [39]. This was verified in [39] which proposed a interturn short-circuit fault diagnosis using a SMO for electric vehicle applications and compared it with the EKF. The fault indicator has been built from the observer estimated value of the windings resistance. The simulation results concluded that the SMO approach is more robust against measurement noise, especially noises in sensors, than the EKF.

In summary, the LO is a simple deterministic approach which does not consider noise and requires low computational power. Opposed to that, the EKF is a stochastic approach designed to overcome the shortcomings of the deterministic LO but it can be less accurate and less robust than the UKF and SMO for systems with nonlinearities or discontinuities.

Despite that, the type of observer to be used will depend on multiple factors such as application, computational resources, and robustness (to parameter variation, noise, and unmodeled dynamics).

This dissertation was aimed at doing something different from the conventional model-based techniques. Usually these techniques compare real sensor data with the one estimated by observers, but here the diagnosis will be performed by applying different signal processing techniques to the DOB output disturbance signal, reference voltages and stator complex power.

3 System Model and Control Strategy

To study the dynamic behaviour of the asymmetrical six-phase PMSM drive, a mathematical model is needed. This section presents the six-phase PMSM drive model and control system and ends with the presentation of a deadtime compensation algorithm.

Six-phase machines have different winding configurations by varying the displacement between each set of three-phase windings. The most common ones are the dual three-phase, asymetrical, and symmetrical machine configurations [40]. Those are well represented in Figure 3.1.

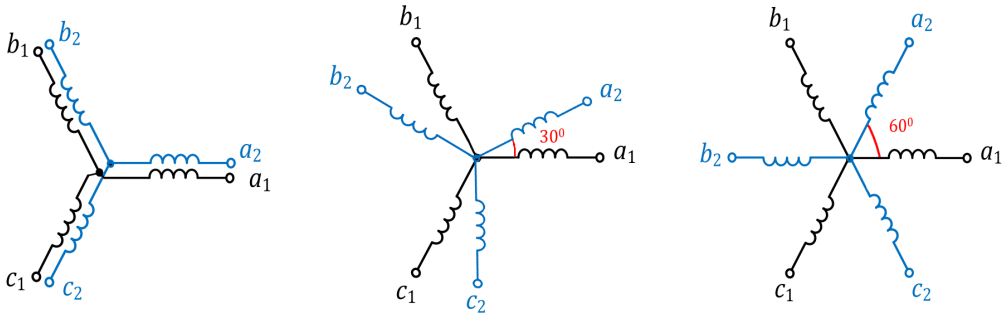

(a) (b) (c)

Figure 3.1: Different configurations of six-phase machines: (a) dual three-phase; (b) asymmetrical; (c) symmetrical. Adapted from [40].

3.1 Healthy Six-Phase PMSM Drive Model

The six-phase PMSM drive model is essential to study the drive dynamic behaviour and develop a robust control system. The equation that describes the asymmetrical six-phase PMSM in the natural reference frame is given by [11]:

$$u_{abc} = \mathbf{R}_s \cdot i_{abc} + \mathbf{L}_{abc} \cdot \frac{di_{abc}}{dt} + e_{abc} \tag{3.1}$$

where $e_{abc}, i_{abc}, u_{abc}, \mathbf{R}_s$, and $\mathbf{L}_{abc}$ are the natural reference frame vectors of the back-EMF, stator currents, stator voltages, resistance matrix and inductance matrix, respectively.

Usually the mathematical models are based on the electrical machine generalized theory where the machine is converted from the natural reference frame into an equivalent model in the synchronous reference frame.

In the asymmetrical six-phase PMSM under study, the machine variables are first transformed from the natural reference frame to the stationary reference frame using the amplitude invariant vector space decomposition (VSD) matrix. It was first proposed in [41] and it made possible to represent a six-phase machine using three subspaces, which are frequently denoted as $\alpha\beta$, xy, and $z1z2$ subspaces.

The VSD matrix used in the six-phase PMSM with asymmetrical winding configuration under study was defined in [11] as:

$$\mathbf{T}_{vsd} = \frac{1}{3}\begin{bmatrix} 1 & \cos\left(\frac{-2\pi}{3}\right) & \cos\left(\frac{-4\pi}{3}\right) & \cos\left(\frac{-\pi}{6}\right) & \cos\left(\frac{-5\pi}{6}\right) & \cos\left(\frac{-9\pi}{6}\right) \\ 0 & -\sin\left(\frac{-2\pi}{3}\right) & -\sin\left(\frac{-4\pi}{3}\right) & -\sin\left(\frac{-\pi}{6}\right) & -\sin\left(\frac{-5\pi}{6}\right) & -\sin\left(\frac{-9\pi}{6}\right) \\ 1 & \cos\left(\frac{-4\pi}{3}\right) & \cos\left(\frac{-2\pi}{3}\right) & \cos\left(\frac{-5\pi}{6}\right) & \cos\left(\frac{-\pi}{6}\right) & \cos\left(\frac{-9\pi}{6}\right) \\ 0 & -\sin\left(\frac{-4\pi}{3}\right) & -\sin\left(\frac{-2\pi}{3}\right) & -\sin\left(\frac{-5\pi}{6}\right) & -\sin\left(\frac{-\pi}{6}\right) & -\sin\left(\frac{-9\pi}{6}\right) \\ 1 & 1 & 1 & 0 & 0 & 0 \\ 0 & 0 & 0 & 1 & 1 & 1 \end{bmatrix}. \tag{3.2}$$

The variables are transformed from the natural reference frame to the stationary reference frame in the following way:

$$\begin{bmatrix} f_\alpha & f_\beta & f_x & f_y & f_{z1} & f_{z2} \end{bmatrix}^T = \mathbf{T}_{vsd} \begin{bmatrix} f_{a_1} & f_{b_1} & f_{c_1} & f_{a_2} & f_{b_2} & f_{c_2} \end{bmatrix}^T \tag{3.3}$$

with $\{f_\alpha, ..., f_{z2}\}$ and $\{f_{a_1}, ..., f_{c_2}\}$ representing the variables in the stationary and natural reference frames, respectively.

The rotation matrix $\mathbf{R}$ is responsible to convert the model from the stationary in an arbitrary reference frame. It is usually chosen the rotor reference frame, rotating at an angular speed w_e. Thus, the rotation matrix is:

$$\mathbf{R} = \begin{bmatrix} \cos(\theta_e) & \sin(\theta_e) & 0 & 0 & 0 & 0 \\ -\sin(\theta_e) & \cos(\theta_e) & 0 & 0 & 0 & 0 \\ 0 & 0 & \cos(\theta_e) & -\sin(\theta_e) & 0 & 0 \\ 0 & 0 & \sin(\theta_e) & \cos(\theta_e) & 0 & 0 \\ 0 & 0 & 0 & 0 & 1 & 0 \\ 0 & 0 & 0 & 0 & 0 & 1 \end{bmatrix} \tag{3.4}$$

where θ_e stands for the rotor electrical position of the six-phase PMSM.

The different variables are transformed to the rotor reference frame in the following way:

$$\begin{bmatrix} f_d & f_q & f_{x'} & f_{y'} & f_{z1} & f_{z2} \end{bmatrix}^T = \mathbf{R} \begin{bmatrix} f_\alpha & f_\beta & f_x & f_y & f_{z1} & f_{z2} \end{bmatrix}^T . \tag{3.5}$$

The resultant six-phase PMSM drive model, in the rotor reference frame, can be expressed as [11]:

$$u_s = \mathbf{R}_s \cdot i_s + \mathbf{L}_s \cdot \frac{di_s}{dt} + \omega_r \cdot \mathbf{J} \cdot \mathbf{L}_s \cdot i_s + e_s \tag{3.6}$$

where e_s, i_s, and u_s have the following format:

$$f_s = \begin{bmatrix} f_d & f_q & f_{x'} & f_{y'} & f_{z1} & f_{z2} \end{bmatrix}^T \tag{3.7}$$

The resistance and inductance matrices in the rotor reference frame are defined as:

$$\mathbf{R}_s = \text{diag}\{R_s, R_s, R_s, R_s, R_s, R_s\} \tag{3.8}$$

$$\mathbf{L}_s = \text{diag}\{L_{dq}, L_{dq}, L_{xy}, L_{xy}, L_{z12}, L_{z12}\} \tag{3.9}$$

where R_s is the resistance of each stator phase winding and the inductances L_{dq}, L_{xy}, and L_{z12} are defined as:

$$L_{dq} = L_s + \sqrt{3M_1 - M_s} \qquad L_{xy} = L_s - \sqrt{3M_1 - M_s} \qquad L_{z12} = L_s + 2M_s \, . \tag{3.10}$$

where L_s is the phase self-inductance, M_s is the mutual inductance between phases within the same set of three-phase windings, and M_1 is the mutual inductance between the phases belonging to different sets of three-phase windings.

3.2 Predictive Current Control with a Disturbance Observer

The current control strategy employed in this study is known as disturbance observer based predictive current control (DOB-PCC).

The current control imposed by a predictive control strategy is characterized by an extremely high bandwidth (typically $\frac{1}{2T_s}$) associated with a small sampling time. A high bandwidth implies that the controller can perform faster and more frequent updates, accurately tracking changes in the reference currents.

In most cases, FCS-MPC strategies utilize a discrete model of the system to forecast the trajectory of the controlled variables. Consequently, the accuracy of predicting these variables relies heavily on the precision of the system model. However, the performance of the control system can also be compromised by parameter mismatch and unmodeled dynamics of the system.

Aiming to improve the performance of the FCS-MPC, a disturbance observer was implemented to eliminate steady-state errors in the current components due to parameter mismatch and also to reduce the current harmonics due to unmodelled dynamics such as back-EMF harmonics and deadtime effects.

Over the years, DOB have been developed and applied in numerous engineering fields for linear systems. On the other hand, when it comes to nonlinear systems, the DOB design leads to a composite controller consisting of a nonlinear controller and a nonlinear disturbance observer [42]. The nonlinear DOB used in this dissertation for robust control was proposed in [12]. The design requires a mathematical model of the six-phase PMSM and then a state space representation of the same dynamic system. The general state-space representation is given as [43]:

$$\begin{cases} \dot{x} = \mathbf{A} \cdot x + \mathbf{B} \cdot u + \mathbf{B} \cdot d_s \\ y = \mathbf{C} \cdot x \end{cases} \tag{3.11}$$

where x, u, and d are the state vector, input and external disturbance respectively. The matrices $\mathbf{A}$, $\mathbf{B}$, and $\mathbf{C}$ describe the dynamics of the system and are defined in [12].

According to [12], adapting the six-phase PMSM drive model in the rotor reference frame given by (3.6), the resultant model including uncertainties is given by:

$$\frac{di_s}{dt} = \mathbf{A} \cdot i_s + \mathbf{B} \cdot u_s - \mathbf{B} \cdot e_s + \mathbf{B} \cdot d_s \,, \tag{3.12}$$

where i_s, u_s, and e_s are the vectors of currents, voltages, and back EMF, respectively. The disturbance vector d_s represents the model uncertainties due to parameter mismatch and other

unmodeled dynamics. Vectors i_s, u_s, e_s, and d_s have the following format:

$$f_s = \begin{bmatrix} f_d & f_q & f_{x'} & f_{y'} \end{bmatrix}^T . \tag{3.13}$$

The elements of d_s cannot be measured, so they have to be estimated with the following exogenous system (given by [12, 42, 43]):

$$\begin{cases} \dot{\xi} = \mathbf{W}\xi \\ d_s = \mathbf{V}\xi \end{cases} \tag{3.14}$$

where ξ and the matrices $\mathbf{V}$ and $\mathbf{W}$ are defined in [12]. Once estimated, the disturbance signal feedbacks the control system to achieve better control performance.

The DOB-PCC strategy implemented has a delay of only $1.5\,T_s$. As a result, the control strategy must first estimate the current vector to instant $k + 0.5$ and then predict the current vector to instant $k + 1.5$. Using the forward Euler method to discretize (3.12), the resultant discrete model is given by:

$$i(k+0.5) = \left[\mathbf{I}_6 + \mathbf{A}\tfrac{T_s}{2}\right] i(k) + \mathbf{B}\frac{T_s}{2}\left[u(k-0.5) - e(k) + \hat{d}(k)\right] . \tag{3.15}$$

The implemented disturbance observer was designed to compensate for parameter errors and unmodeled dynamics such as the deadtime in the power converters and back-EMF harmonics. As described in [12, 44], the deadtime is responsible for the appearance of harmonics at the fundamental frequency, mapped in the $\alpha\beta$ subspace, and 5th and 7th order harmonics mapped in the xy subspace. The spectral analysis, of the current in the xy subspace (i_{xy}) presented in Figure 3.2 show the reduced harmonic content in i_{xy}, mainly in the amplitude of the 5th and 7th order harmonics, due to the DOB compensation.

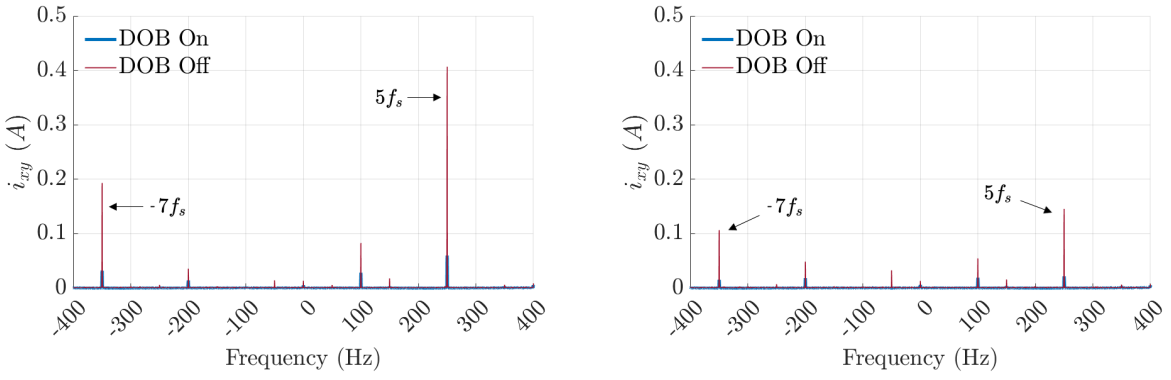

Figure 3.2: Experimental results for i_{xy}, when the healthy six-phase PMSM operates at 1500 rpm with rated load: (a) motoring mode; (b) generating mode.

3.3 Inverter Deadtime Compensation Method

Deadtime in power converters refers to the interval of time during which both the upper and lower switches of a given inverter leg are turned off to prevent short-circuits. This causes a short time interval where no voltage is applied to the machine which leads to a difference between the reference voltage and the real voltage applied to the machine windings.

As mentioned earlier, the DOB integrated into the control system plays a crucial role in the compensation of harmonics at the fundamental frequency, in the $\alpha\beta$ subspace, and 5th and 7th order harmonics mapped in the xy subspace. The compensation is mainly made by increasing the reference voltage component at fundamental frequency in the $\alpha\beta$ subspace, and 5th and 7th order harmonics in the xy subspace.

To obtain more realistic values of the reference voltages the following deadtime compensation method, adapted from [44], was applied to the measured signals.

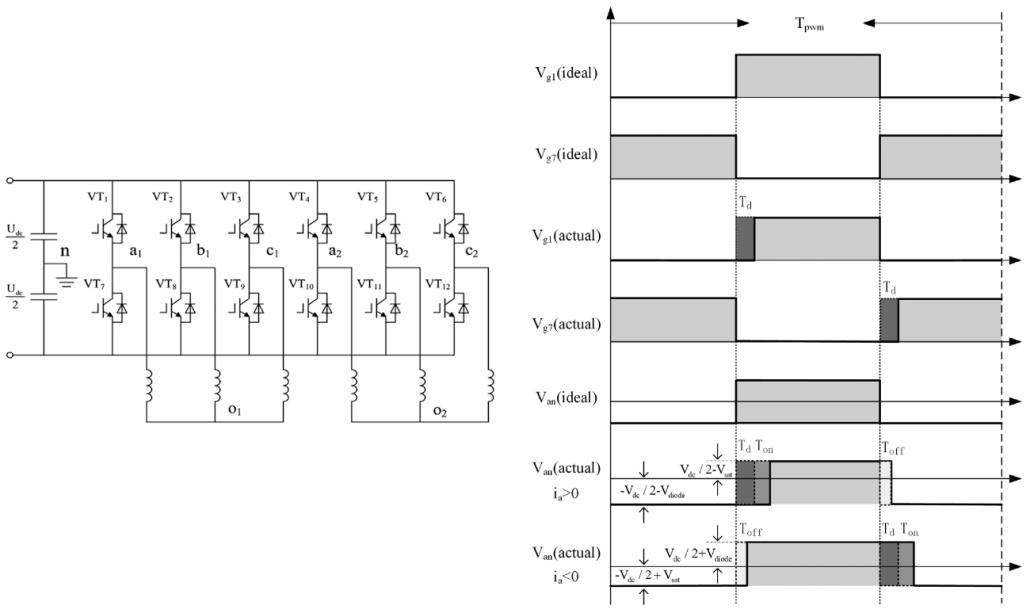

Figure 3.3: Topological structure of a six-phase inverter, and gate signals and pole voltages under ideal and under deadtime conditions. Adapted from [44]

The voltage error caused by the deadtime effect (ΔV_{an}) within a switching period can be expressed as:

$$\Delta V_{\text{an}} = s(i_{\text{an}}) \cdot V_d \tag{3.16}$$

where i_{an} is the current in the considered phase, and V_d is given by:

$$V_d = \frac{T_d + T_{on} - T_{off}}{T_s} \left(V_{dc} - V_{sat} + V_{diode}\right) - V_{diode} + V_{sat} \,, \tag{3.17}$$

where T_{on}, T_{off}, T_d, and T_s are the turn-on time, and turn-off time of the IGBTs, the deadtime, and the switching period, respectively. V_{dc}, V_{sat}, V_{diode} are the bus voltage, switch saturation voltage, and diode forward voltage, respectively.

The sign function $s(i_{an})$ can be expressed as:

$$s(i_{an}) = \begin{cases} 1, & i_{an} > 0 \\ -1, & i_{an} < 0 \end{cases} . \tag{3.18}$$

The deadtime voltage error in the natural reference frame is given by:

$$\Delta V_{abc} = \begin{bmatrix} \Delta V_{a1} \\ \Delta V_{b1} \\ \Delta V_{c1} \\ \Delta V_{a2} \\ \Delta V_{b2} \\ \Delta V_{c2} \end{bmatrix} = \frac{1}{3} \begin{bmatrix} 2 & -1 & -1 & 0 & 0 & 0 \\ -1 & 2 & -1 & 0 & 0 & 0 \\ -1 & -1 & 2 & 0 & 0 & 0 \\ 0 & 0 & 0 & 2 & -1 & -1 \\ 0 & 0 & 0 & -1 & 2 & -1 \\ 0 & 0 & 0 & -1 & -1 & 2 \end{bmatrix} \begin{bmatrix} s(i_{a1})V_d \\ s(i_{b1})V_d \\ s(i_{c1})V_d \\ s(i_{a2})V_d \\ s(i_{b2})V_d \\ s(i_{c2})V_d \end{bmatrix} \tag{3.19}$$

Taking into account (3.3), the deadtime voltage error in the stationary reference frame is obtained by the following equation:

$$\Delta V_{\alpha\beta} = \mathbf{T}_{vsd} \cdot \Delta V_{abc} \,, \tag{3.20}$$

where $\Delta V_{\alpha\beta}$ and ΔV_{abc} are the vectors of the voltages in the stationary and natural reference frame respectively.

$$\Delta V_{\alpha\beta} = \begin{bmatrix} \Delta V_\alpha & \Delta V_\beta & \Delta V_x & \Delta V_y & \Delta V_{z1} & \Delta V_{z2} \end{bmatrix}^T \tag{3.21}$$

The reference voltage is different from the real voltage applied to the machine windings due to different phenomena such as deadtime. In order to obtain more realistic values of the reference voltages in the $\alpha\beta$ subspace, the deadtime compensation method was applied by subtrarcting the filtered deadtime voltage error to the filtered reference voltages.

Due to the high DC-link voltage in the PMSM drive, when the algorithm is applied to normal operating conditions (with $T_d = 2.2\,\mu s$), the voltage error due to deadtime has a component at the fundamental frequency of $14\,V$, which represents a considerable error especially at lower speeds when the PMSM supply voltage is lower, making the impact of deadtime in the drive more noticeable. Table 3.1 shows the evolution of the amplitude of the fundamental component of the

voltage in the $\alpha\beta$ subspace for various speeds, with a compensation of $D_t = 2.2\,\mu s$ ($u^{f_s}_{\alpha\beta,comp.}$) and without deadtime compensation ($u^{f_s}_{\alpha\beta}$).

Table 3.1: Evolution of $u^{f_s}_{\alpha\beta}$ and $u^{f_s}_{\alpha\beta,comp.}$ (with $T_d = 2.2\,\mu s$) with rotor speed.

Rotor speed (rpm)	Motor			Generator		
	$u^{f_s}_{\alpha\beta}$ (V)	$u^{f_s}_{\alpha\beta,comp.}$ (V)	Error	$u^{f_s}_{\alpha\beta}$ (V)	$u^{f_s}_{\alpha\beta,comp.}$ (V)	Error
300	77.2	63.4	17.9 %	41.4	55.3	33.5 %
600	137.3	123.2	10.3 %	103.2	117.5	13.8 %
900	193.7	181.0	6.6 %	164.5	178.8	8.69 %
1200	260.0	247.3	4.9 %	221.3	235.6	6.5 %
1500	319.4	307.9	3.6 %	281.6	296.7	5.4 %

Table 3.1 reveals that high errors are obtained due to the deadtime at lower rotor speeds.

Figure 3.4 presents the deadtime voltage error in the $\alpha\beta$ subspace obtained with the used algorithm. According to the Fourier series expressed in [44], the voltage deadtime error in the $\alpha\beta$ subspace has components at the fundamental supply frequency, as well as at $11f_s$ and $13f_s$ (see Figure 3.4b).

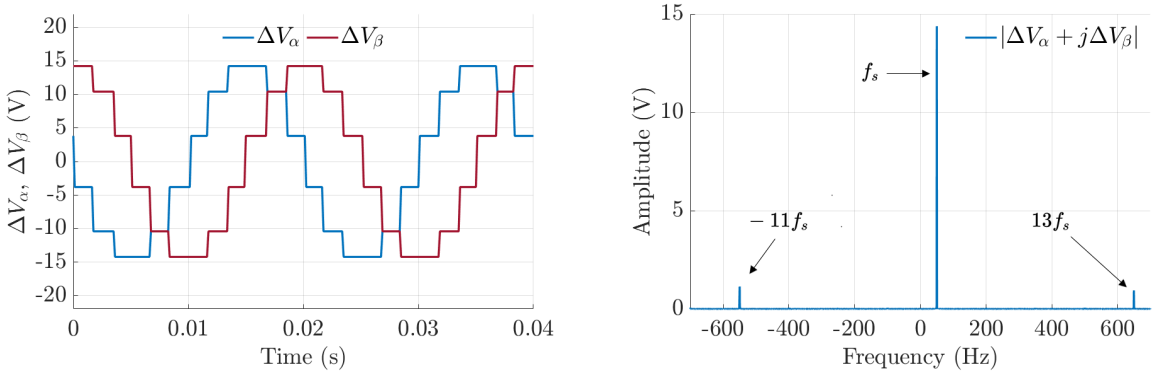

(a) (b)

Figure 3.4: Voltage error in the $\alpha\beta$ subspace due to a deadtime of $T_d = 2.2\,\mu s$ when $V_{dc} = 650\,V$: (a) time signals; (b) voltage space vector spectrum.

4 Interturn Short-Circuit Fault Diagnosis Using the DOB

This chapter presents the system model under the presence of interturn short-circuit faults in the six-phase PMSM and the approaches that will be applied in order to diagnose this type of fault.

4.1 System Model Under Faulty Conditions

An interturn short-circuit fault occurs when the current flows through an unintended path in a machine specific phase.

The modeling of a PMSM with this type of fault consists in splitting the winding of the damaged phase into two parts, the healthy and the faulty one as presented in Figure 4.1, which was adapted to a six-phase PMSM taking into account the faulty model presented in [45]. The healthy part is characterized by the healthy winding resistance, inductance and mutual inductances, while the faulty part is characterized by the faulty resistance, inductance and mutual inductance between the shorted turns and other phase windings. The short-circuit current i_{sc} is characterized by a short-circuit resistance in parallel with the faulty part and relates with the other currents by the following expression:

$$i_{sc} = i_{a_1} - i_{a_1 f} \, . \tag{4.1}$$

The magnitude of the short-circuit current depends on various factors such as the number of turns involved in the short-circuit and the contact resistance of the short-circuit itself. For example, considering two equal PMSMs it is possible to have the same amount of short-circuited turns and different short-circuit currents due to the short-circuit resistance. In practice, when testing the short-circuit the contact resistance is never zero. Instead, a resistance is added to limit the current and avoid machine damage.

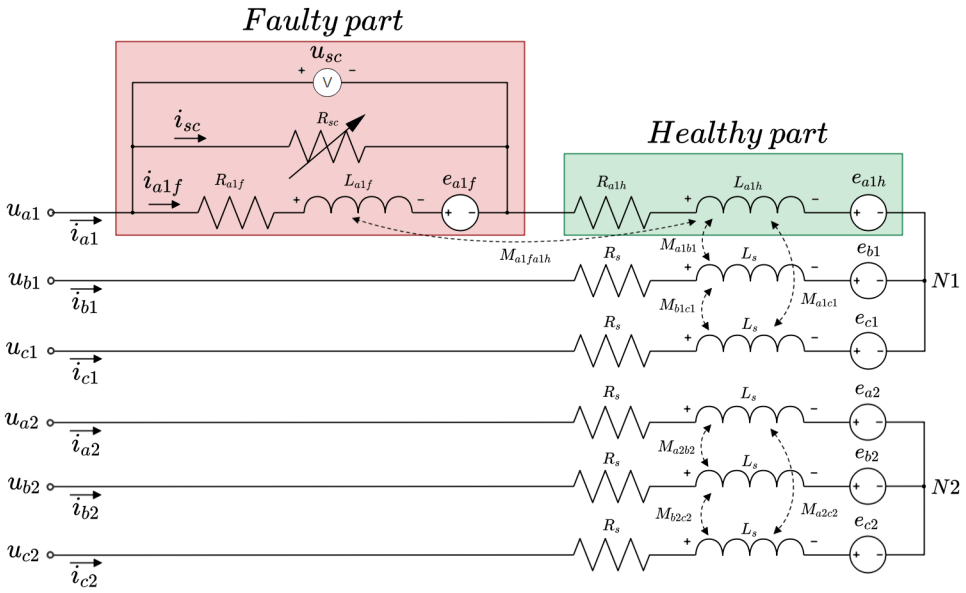

Figure 4.1: Electrical model of a six-phase PMSM with an interturn short-circuit in phase a_1. Adapted from [45].

According to Figure 4.1 and [28]:

$$\begin{cases} \mu = \frac{N_{sc}}{N_{tot}} \\ R_{a_1 f} = \mu R_s \\ R_{a_1 h} = (1-\mu) R_s \end{cases} \tag{4.2}$$

where μ, N_{sc}, N_{tot}, $R_{a_1 f}$, $R_{a_1 h}$, are the winding short-circuit ratio, turns in the short-circuit, total winding turns, faulty resistance, and the healthy resistance, respectively.

4.2 Proposed Fault Diagnostic Methods

Different non-invasive fault diagnostic methods that can detect interturn short-circuits in six-phase PMSM drives are presented in this section.

In a predictive current control strategy, the motor currents are regulated to track the respective reference values by adjusting the voltage applied to the machine. As a result, a current based fault indicator may not be significantly noticeable in this context, but it will be particularly evident in the refrence voltages.

The fault will also affect the estimated disturbances d_s. If the estimated disturbance is significantly larger than the expected disturbance in the absence of a fault, this may indicate the presence of an interturn short-circuit fault.

Different from the conventional model-based techniques using observers, the fault diagnosis method in this dissertation will be implemented as represented in Figure 4.2, by applying FFTs to multiple variables which will be explored in the following subsections.

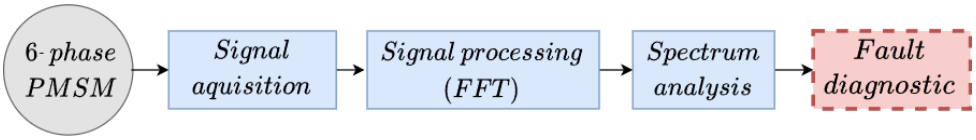

Figure 4.2: Fault diagnostic technique diagram, adapted from [15].

4.2.1 Brief Considerations

This dissertation proposes the use of quantities in the $\alpha\beta$ subspace as the preferred choice among the various subspaces available for analysis. This specific subspace has been predominantly employed for the purpose of fault diagnosis. Comparing the frequency spectrum of both DOB output and reference voltages in $\alpha\beta$ subspace with the xy subspace, becomes clear that the first one reveals a substancial increase in the negative sequence component while the other one has minor and low amplitude changes and presents a less well-defined spectrum. The xy subspace is particularly characterized by the prevalence of the 5th and 7th harmonics, both of which are influenced by various factors such as deadtime effects and back-EMF harmonics.

Furthermore, the $\alpha\beta$ subspace not only serves as an effective domain for fault diagnosis but also offers advantage over the rotor reference frame dq due to easier fault location.

Besides the DOB output and reference voltage methods, the stator complex power within the dq subspace was also analyzed for comparative analysis. The stator complex power exclusive application within the dq subspace is notable due to the remarkably close resemblance between the results obtained in this subspace and those derived in the stationary reference frame. This congruence eliminates the need for any subspace transformation, simplifying the analysis procedure significantly.

4.2.2 DOB Output Spectrum Analysis in the $\alpha\beta$ Subspace

The DOB output was employed in the diagnosis of interturn short-circuits by studying the behaviour of its negative sequence component, at fundamental frequency in the $\alpha\beta$ subspace ($d_{\alpha\beta}^{-f_s}$). For that purpose, the spatial vector of the DOB is needed. It is given as:

$$\underline{d}_{\alpha\beta} = d_\alpha + j d_\beta \, . \tag{4.3}$$

It should be noted that $d_{\alpha\beta}^{-f_s}$ may appear even in an healthy machine due to intrinsic machine asymmetries and is commonly referred as residual asymmetries. The stator windings of a PMSM

are designed to be symmetrically balanced, ensuring smooth and efficient operation. However, factors such as an uneven airgap between the stator and rotor can lead to residual asymmetries.

Considering the presence of residual asymmetries, it becomes crucial to account for them when developing a fault diagnosis technique. By understanding and addressing these asymmetries, more accurate and effective fault diagnosis methods can be developed and implemented. The characterization of residual asymmetries in the machine requires conducting extensive tests encompassing a wide range of speed and load operating points. Consequently, an ideal diagnostic technique should be able to operate independently of the machine residual asymmetry.

With this said, two different approaches were implemented: one is based on the analysis of the amplitude of the negative sequence component of the DOB in the $\alpha\beta$ supspace, and the other one decouples that component from machine residual asymmetries in the following way:

$$\underline{d}_{\alpha\beta,sc}^{-f_s} = \underline{d}_{\alpha\beta,f}^{-f_s} - \underline{d}_{\alpha\beta,h}^{-f_s} \tag{4.4}$$

where $\underline{d}_{\alpha\beta,sc}^{-f_s}$, $\underline{d}_{\alpha\beta,f}^{-f_s}$, and $\underline{d}_{\alpha\beta,h}^{-f_s}$, are respectively the short-circuit (decoupled from residual asymmetries), faulty and healthy disturbance observer negative sequence components, at $-f_s$, in the $\alpha\beta$ subspace.

In fault diagnosis, it is important not only to detect the faults but also to quantify their extension. For that purpose, severity factors (SFs) are usually defined, giving the measure of how serious those faults are. Since the DOB output fundamental component depends on several factors such as deadtime and parameter errors, the following severity factor was adopted:

$$SF_{d_{\alpha\beta}} = \frac{d_{\alpha\beta,sc}^{-f_s}}{u_{\alpha\beta,f}^{f_s}} \tag{4.5}$$

where $\underline{u}_{\alpha\beta,f}^{f_s}$ is the reference voltage space vector at the fundamental frequency f_s, in the $\alpha\beta$ subspace in the faulty machine.

Given that the disturbance observer implemented in the control is in the synchronous dq reference frame, there is a need to convert it to the stationary $\alpha\beta$ reference frame by applying the inverse rotation matrix. Despite being an additional step, it is easily implemented and the stationary frame enables easier fault location.

4.2.3 Stator Voltage Spectrum Analysis in the $\alpha\beta$ Subspace

The negative sequence component of the stator voltage, at the fundamental frequency in the $\alpha\beta$ subspace ($u_{\alpha\beta}^{-f_s}$) has already been used as an interturn short-circuit indicator in both five and six-phase PMSMs in [46] and [47] respectively. The amplitude of this component has revealed to be more reliable in the diagnosis of this type of fault than other spectral components.

In order to study $u_{\alpha\beta}^{-f_s}$, the spatial vector needed is obtained as follows:

$$\underline{u}_{\alpha\beta} = u_\alpha + ju_\beta \,. \tag{4.6}$$

Once $\underline{u}_{\alpha\beta}$ is obtained, the FFT is applied and the negative sequence component is extracted. Real world machines have inherent asymmetries. The component under study is decoupled from residual assymetries in the following way:

$$\underline{u}_{\alpha\beta,sc}^{-f_s} = \underline{u}_{\alpha\beta,f}^{-f_s} - \underline{u}_{\alpha\beta,h}^{-f_s} \tag{4.7}$$

where $\underline{u}_{\alpha\beta,sc}^{-f_s}$, $\underline{u}_{\alpha\beta,f}^{-f_s}$, and $\underline{u}_{\alpha\beta,h}^{-f_s}$, are, respectively, the short-circuit (decoupled from residual asymmetries), faulty and healthy reference voltage negative sequence components, at $-f_s$ in the $\alpha\beta$ subspace.

The increase of $\underline{u}_{\alpha\beta,sc}^{-f_s}$ is primarily influenced by i_{sc}, which depends on both the short-circuit resistance and the voltage between the short-circuited turns. This voltage, in turn, relies on the PMSM back-EMF, which is directly influenced by the rotor speed.

Similarly to (4.5) the following severity factor was implemented:

$$SF_{u_{\alpha\beta}} = \frac{u_{\alpha\beta,sc}^{-f_s}}{u_{\alpha\beta,f}^{f_s}} \tag{4.8}$$

This severity factor becomes almost independent of the PMSM rotor speed which has a proportional relationship with the voltage applied to the machine.

4.2.4 Complex Aparent Power Spectrum Analysis in the dq Subspace

Diagnostic methods such as the on presented in [48] use the spectrum analysis of active and reactive powers, separately.

Aiming for something different, the fault diagnostic method presented in this subsection consists in the analysis of stator complex apparent power ($\underline{s}$), by the identification of its $-2f_s$ component in the dq subspace. The advantage of the implemented method is that it combines information from both active and reactive power into a single indicator. It is defined as the vector sum of active and reactive powers (p and q respectively).

$$\underline{s}_{dq} = p_{dq} + jq_{dq} \tag{4.9}$$

Once the current and voltage signals are obtained in phase coordinates, the VSD transformation is applied to obtain the signals in the $\alpha\beta$ and xy subspaces, hereupon, the rotation

matrix is applied to obtain the current and voltage in dq and $x'y'$ coordinates. The stator active and reactive powers in the dq reference frame are calculated according to (4.10) and (4.11) [48, 49, 50].

$$p_{dq} = 3(u_{ds}i_{ds} + u_{qs}i_{qs}) \tag{4.10}$$

$$q_{dq} = 3(u_{qs}i_{ds} - u_{ds}i_{qs}) \tag{4.11}$$

For this method, the following severity factor was adopted:

$$SF_{s_{dq}}(pu) = \frac{\underline{s}_{dq,f}^{-2} - \underline{s}_{dq,h}^{-2}}{S_b}\,, \tag{4.12}$$

where $\underline{s}_{dq,f}^{-2}$, $\underline{s}_{dq,h}^{-2}$, are respectively the faulty and healthy stator complex apparent power vectors, obtained by the $-2f_s$ component in the dq subspace. The base power S_b is defined as the rated power extracted from the machine nameplate.

5 Simulation and Experimental Results

This chapter validates the methods proposed in the previous chapter through a cosimulation using Ansys software and experimental results obtained with the six-phase PMSM controlled with a DOB-PCC strategy. The cosimulation model is briefly described, then the different components of the electric drive are presented and a brief introduction is given on how the short-circuits were implemented. Finally, the various experimental results are presented and analyzed.

The six-phase PMSM under study has 208 turns per phase, which are distributed by 8 coils placed along the stator slots of the machine (more details on coil connections in the Appendix C, Figure C.9). Each coil has 26 turns and the short-circuits were always introduced in the first coil of each phase, as presented in Figure 5.1.

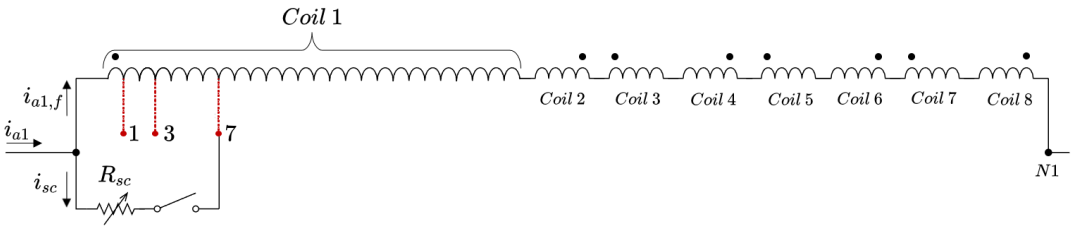

Figure 5.1: Representation of the stator winding of phase a_1 with a short-circuit.

5.1 Considerations about the Cosimulation Model

Finite element simulations have proven to be an indispensable tool in the study of PMSMs and their associated faults. These simulations offer numerous advantages, providing valuable insights and complementing experimental investigations, however this comes at a cost of long simulation times.

To validate the experimental results presented in the following subsections, over 30 hours of

simulation time was allocated for finite element analysis using Ansys TwinBuilder.

The DOB-PCC strategy proposed in [12] was developed in Matlab/Simulink and then exported to C programming language to run along the six-phase PMSM model in Ansys. The interface of this model is presented in Appendix B.

The Ansys model implemented runs with a sampling time of $T_s = 125\,\mu s$, features a balanced power supply voltage system, as well as the absence of deadtime and machine residual asymmetries.

In order to achieve results similar to the experimental ones, the short-circuits were introduced in the first coil of each phase (as presented in Figure 5.2) using a fault resistance of $R_{sc} = 0.5\,\Omega$ to obtain similar values of short-circuit current as in the experimental data.

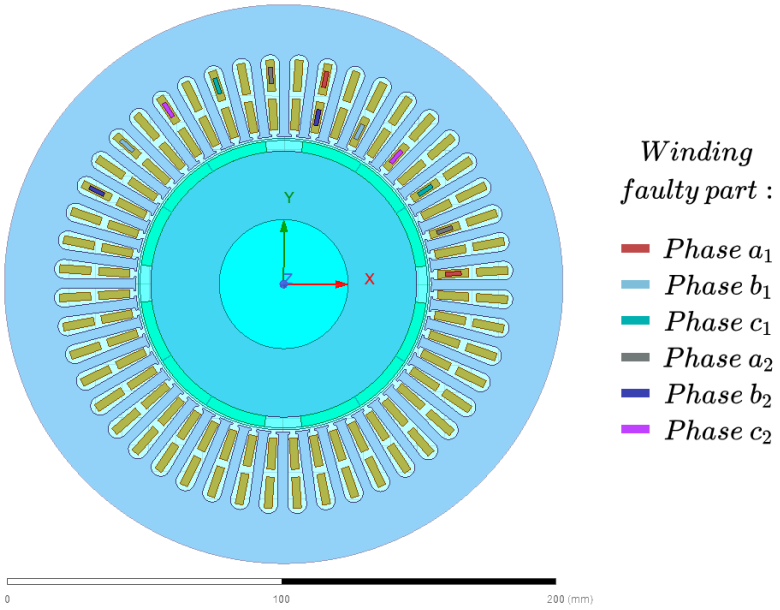

Figure 5.2: Ansys cross-sectional view of the six-phase PMSM with 7 turns in short-circuit in the first coil of each phase.

5.2 Definition of the Experimental Setup

To validate the proposed fault diagnostic methods, several experimental results were obtained from a 4 kW six-phase PMSM. The six-phase PMSM is mechanically coupled to an auxiliary induction motor powered by a frequency converter. Additionally, a 2048 ppr incremental encoder measures the rotor position.

The proposed control strategy is implemented in a dSPACE DS1103 control platform using MATLAB/Simulink. After each control cycle, the DS1103 platform sends the leg duty cycles to the cRIO-9066 NI realtime control platform. The IGBTs control signals are generated by the cRIO N9066 due to the higher temporal resolution, that the DS1103 lacks. However, since

the power converters have 12 IGBTs, it requires 12 PWM outputs to generate the appropriate switching patterns.

The controller sampling period in the implemented control strategy is $T_s = 125\,\mu s$.

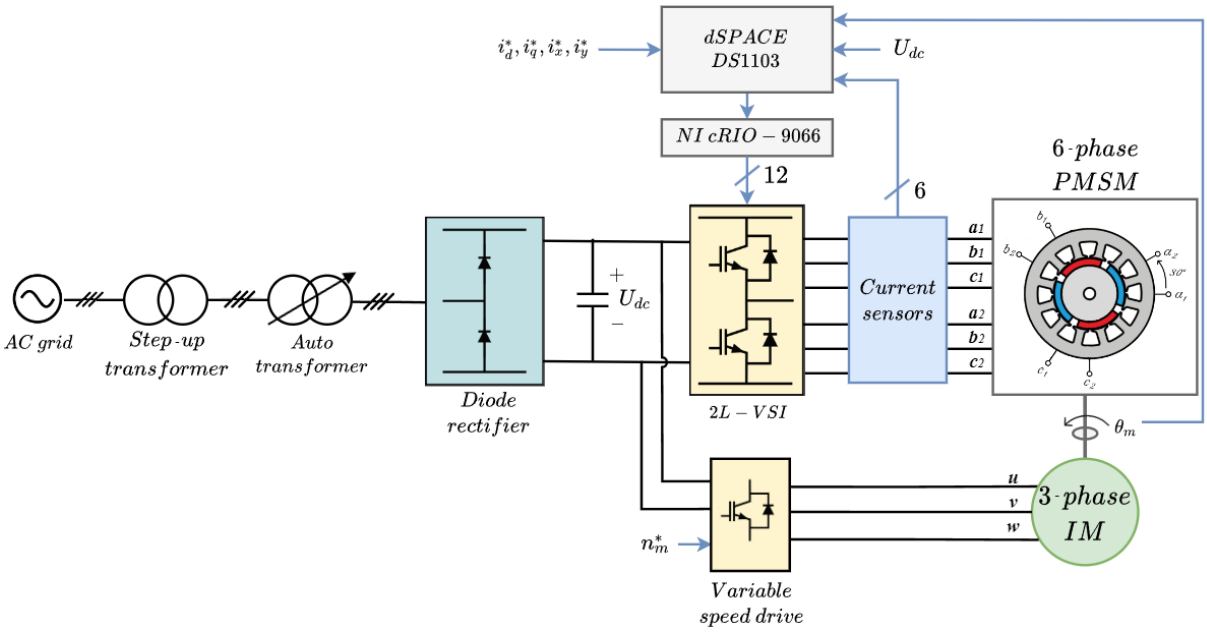

Figure 5.3: Experimental setup diagram.

For data acquisition and real-time visualization during the experimental tests, the Control Desk interface was employed. Within the control panel presented in Appendix C, Figure C.8, the user can adjust various parameters of the electric drive, such as the load level, rotor speed, and parameter values.

The experimental data used in this thesis (both healthy and faulty data) was obtained along a time window of 4 s, in steady-state conditions. Each data acquisition was synchronized with the ascending slope of the initial rotor position provided by the encoder.

The majority of the interturn short-circuits were introduced in phase a_1, however in order to locate the faulty phase these were extended to each one of the six-phase PMSM phases.

The data sampled from phase a_1 covers 1,3, and 7 short-circuited turns at five different speeds: 1500 rpm, 1200 rpm, 900 rpm, 600 rpm, and 300 rpm. For each speed five load levels were considered: 100%, 75%, 50%, 25%, and no load condition in both motoring and generating modes.

For the phases other than phase a_1, the data only covers 7 short-circuited turns with the six-phase PMSM operating at 1200 rpm with rated load in both motoring and generating modes.

5.3 Preliminary Results

Figure 5.4 shows the current waveforms in phase a_1: healthy winding (i_{a_1}), faulty winding ($i_{a_1,f}$) and in the short-circuit (i_{sc}).

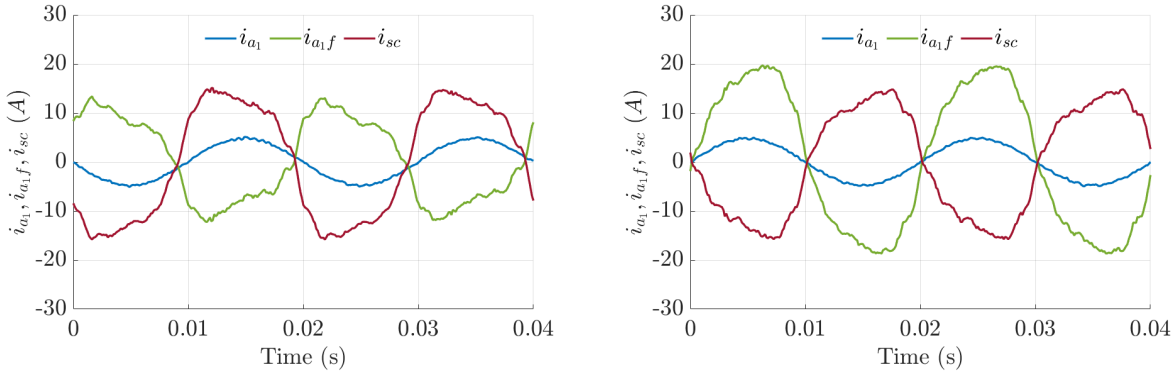

(a) (b)

Figure 5.4: Experimental results of $i_{a_1}, i_{a_1 f}, i_{sc}$, with $N_{sc} = 7$ in phase a_1 with the PMSM operating at 1500 rpm with rated load: (a) motoring mode; (b) generating mode.

The short-circuit current frequency spectrum is presented in Figure 5.5. This current is characterized by odd harmonics, mainly the third.

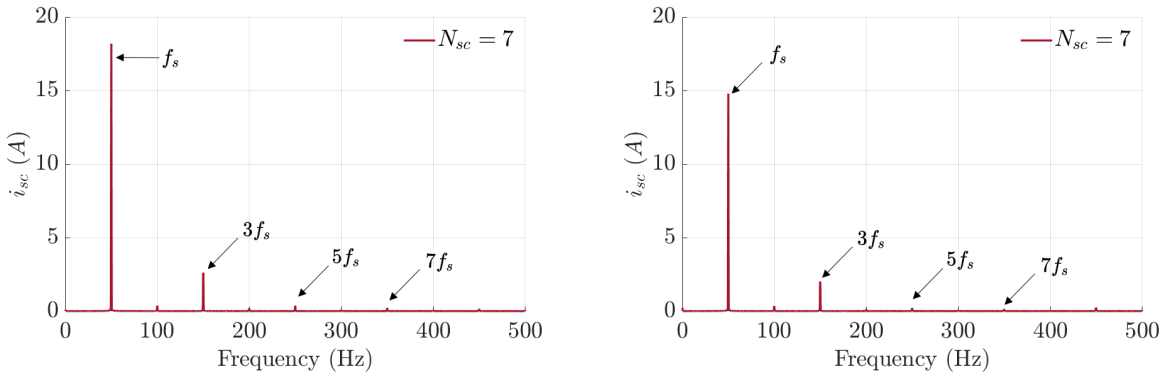

(a) (b)

Figure 5.5: Experimental results for the frequency spectrum of i_{sc}, with $N_{sc} = 7$ in phase a_1, with the PMSM operating at 1500 rpm with rated load: (a) motoring mode; (b) generating mode.

As expected the fault current obtained when the six-phase PMSM operates in generating mode is lower than in motoring mode. The short-circuit current depends on the the short-circuit resistance and the voltage between the short-circuited turns which is smaller in generating mode. This is due to the voltage in the machine terminals only being dependent on the permanent magnets.

5.4 DOB Output Spectrum Analysis in the $\alpha\beta$ Subspace

This section presents both simulation and experimental results for the DOB output component, at a frequency of $-f_s$, in the $\alpha\beta$ subspace ($d_{\alpha\beta}^{-f_s}$).

The time evolution of the DOB output in the stationary reference frame is presented in Figures 5.7 and 5.6 for cosimulation and experimental data, respectively.

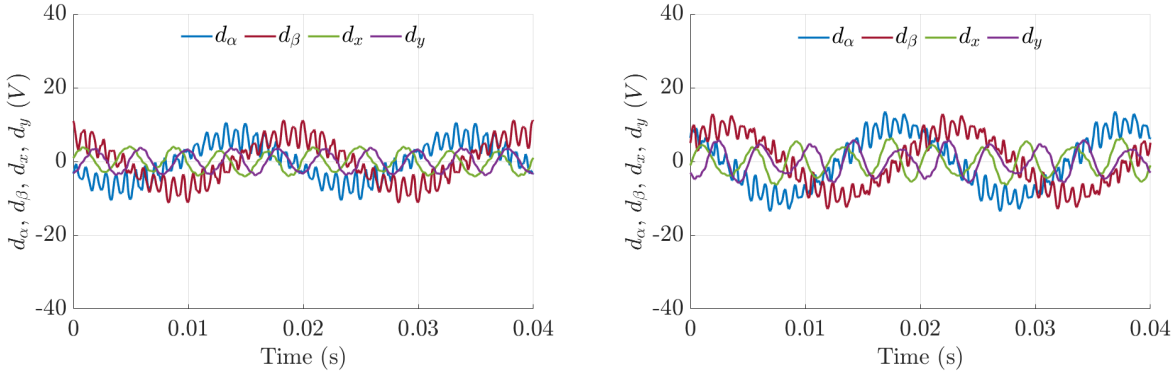

Figure 5.6: Cosimulation DOB output signals, in the stationary frame, with the healthy PMSM operating at 1500 rpm with rated load: (a) motoring mode; (b) generating mode.

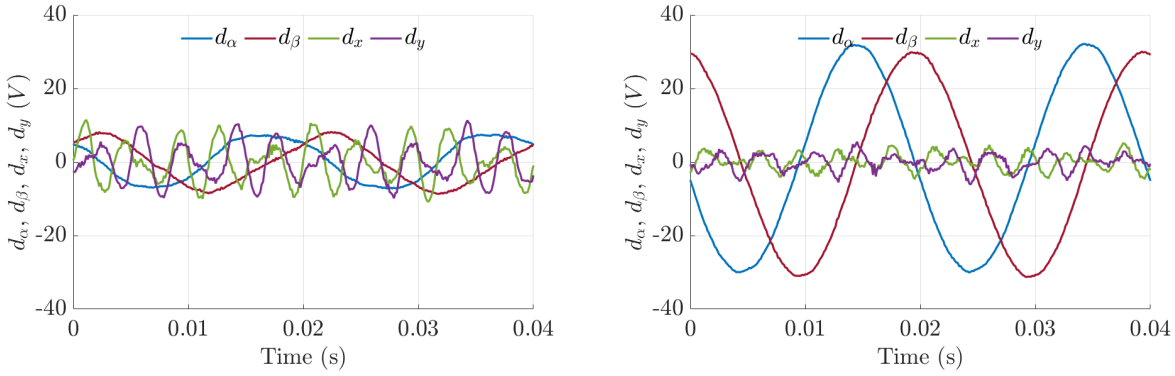

Figure 5.7: Experimental DOB output signals, in the stationary frame, with the healthy PMSM operating at 1500 rpm with rated load: (a) motoring mode; (b) generating mode.

By inspecting Figures 5.6 and 5.7, becomes evident that there exists greater distortion along the xy subspace in comparison to the $\alpha\beta$ subspace. While the DOB compensates mainly for components at fundamental frequency in $\alpha\beta$ subspace, in the xy subspace the DOB compensates for 5th and 7th order harmonics. Additionally, in contrast to the experimental data, the cosimulation DOB output signals present a noticeable high frequency component in the $\alpha\beta$ subspace.

It is also evident a huge amplitude difference in the DOB output signal, in the $\alpha\beta$ subspace, when the six-phase PMSM operates in motoring and generating modes. Even when accounting for deadtime and parameter errors, this discrepancy in the DOB output signal persists and is absent in the cosimulation data from Figure 5.6.

This dissertation explores mainly the $\alpha\beta$ subspace components for the diagnosis of interturn short circuits.

Figures 5.8 and 5.9 present the frequency spectrum of $\underline{d}_{\alpha\beta}$ and $\underline{d}_{xy}$, respectively.

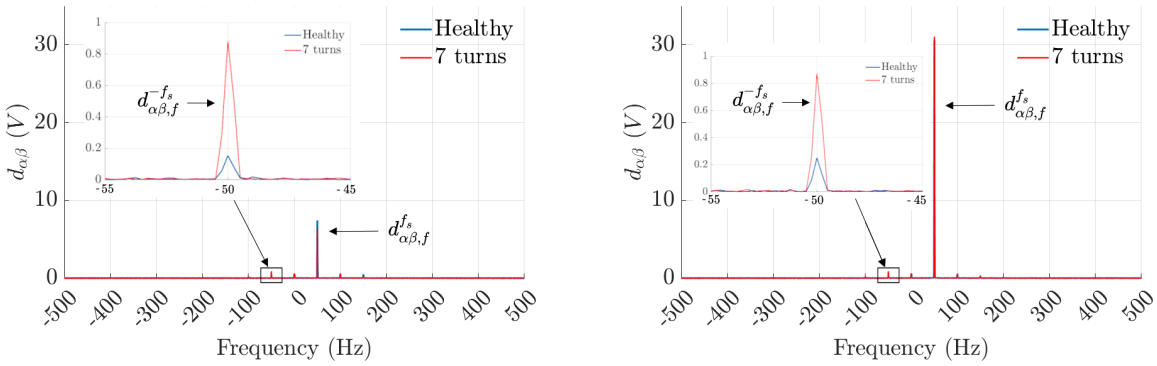

(a) (b)

Figure 5.8: Experimental $\underline{d}_{\alpha\beta}$ spectrum, considering the PMSM drive operating at 1500 rpm with rated load and 7 short-circuited turns in phase a_1: (a) motoring mode; (b) generating mode.

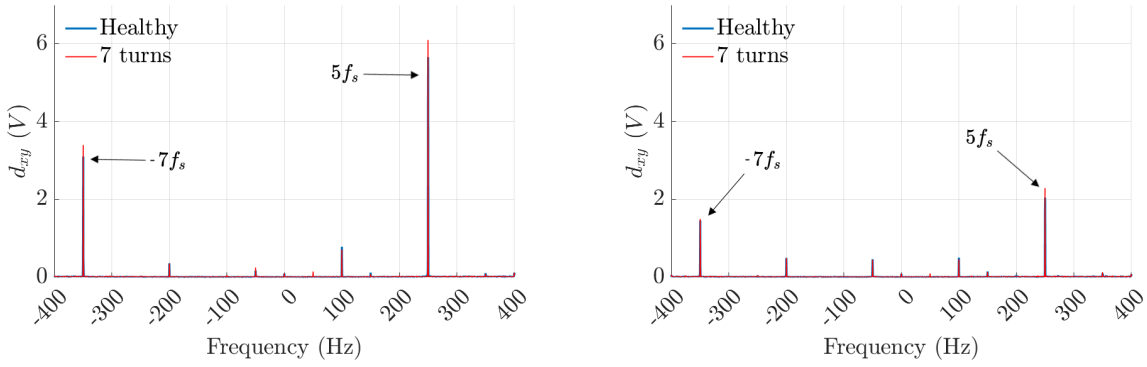

(a) (b)

Figure 5.9: Experimental $\underline{d}_{xy}$ spectrum with the PMSM operating at 1500 rpm, at rated load with 7 short-circuited turns in phase a_1: (a) motoring mode; (b) generating mode.

By inspecting Figure 5.8, in addition to the residual asymmetry of the healthy six-phase PMSM, it is also noticeable a clear increase in $d^{-f_s}_{\alpha\beta}$ related to the interturn short-circuit. When it comes to $\underline{d}_{xy}$ spectrum, in Figure 5.9, although visible some increase in certain spectral components such as the 5th harmonic, it is a small increase considering the worst case scenario

with 7 turns at 1500 rpm, and this spectral component, as previously said, is affected by different phenomena such as the deadtime and back-EMF harmonics.

Inspecting the frequency spectrum of the DOB output spatial vector in the $\alpha\beta$ subspace it is noticeable an overall cleaner spectrum with well defined low amplitude frequency components.

The simulation results in Figure 5.10 validate the $d_{\alpha\beta}^{-f_s}$ increase when the six-phase PMSM is under interturn short-circuits. It is a expected result since the increase of the component is directly related to this type of fault. In generating operation the component has lower amplitude value compared to motoring mode, due to the lower short-circuit current in the generating mode of operation.

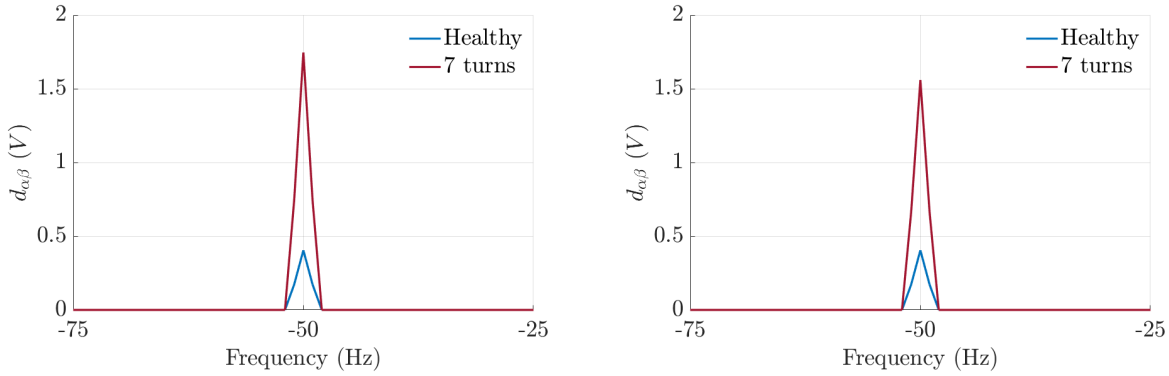

Figure 5.10: Simulation results for $d_{\alpha\beta}^{-f_s}$, considering the PMSM drive operating at 1500 rpm and rated load, with 7 short-circuited turns ($R_{sc} = 0.5\,\Omega$) in phase a_1: (a) motoring mode; (b) generating mode.

Figure 5.11 presents the experimental results for $d_{\alpha\beta}^{-f_s}$.

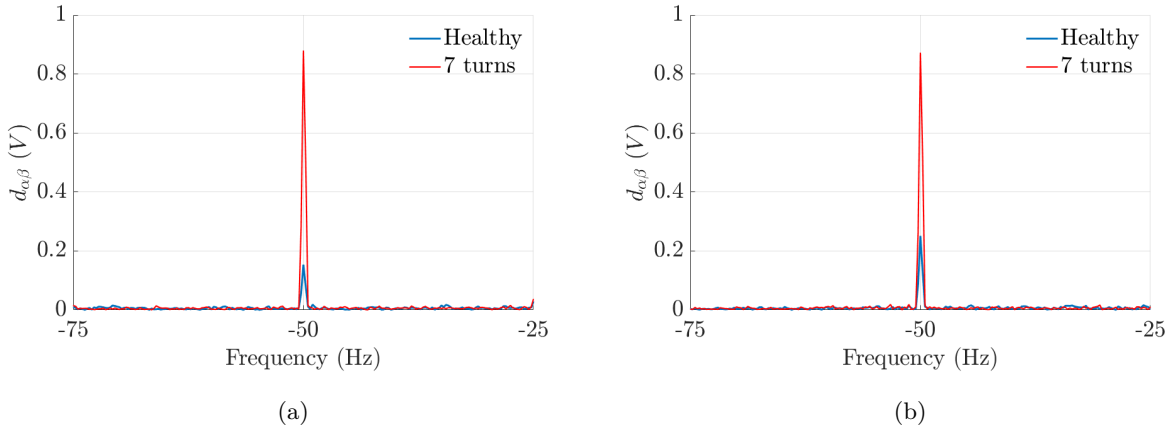

Figure 5.11: Experimental results for $d_{\alpha\beta}^{-f_s}$, considering the PMSM drive operating at 1500 rpm at rated load with 7 short-circuited turns in phase a_1: (a) motoring mode; (b) generatoing mode.

The results validate the simulation results and the same conclusions can be drawn, however

it was noted that in the experimental results, $d_{\alpha\beta}^{-f_s}$ has a lower amplitude in both healthy and faulty states, when compared to the cosimulation results. Several hypotheses were considered for this discrepancy between the cosimulation and experimental results, such as the deadtime effect and parameter errors in experimental results, however, as it will be confirmed in subsection 5.4.3, the discrepancy is not due to these factors.

5.4.1 Influence of the Short-Circuit Current

To study the effects of the amplitude of the short-circuit current in $d_{\alpha\beta}^{-f_s}$, several tests were conducted with both 3 and 7 short-circuited turns in phase a_1, with the PMSM drive operating at 1200 rpm and rated load. The only variable that was changed in these tests was the fault resistance, to obtain different short-circuit current values.

Figure 5.12 shows the variation of $d_{\alpha\beta}^{-f_s}$ in motor and generator operation with 3 and 7 short-circuited turns, respectively.

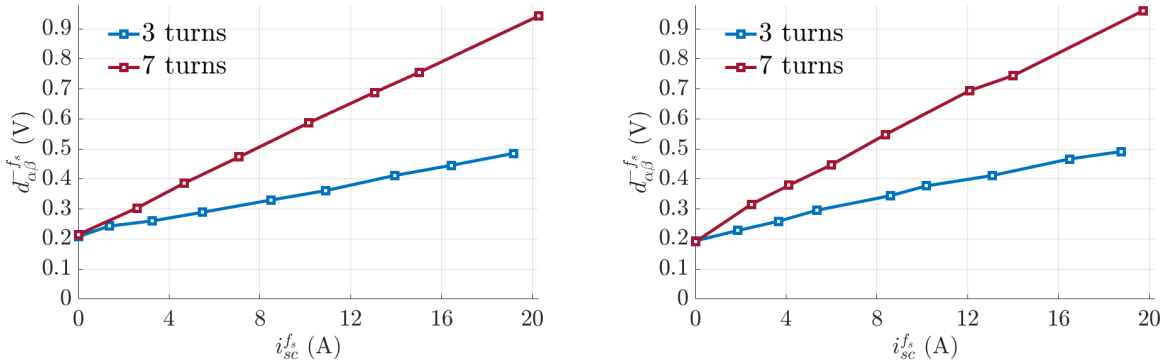

Figure 5.12: Evolution of the experimental $d_{\alpha\beta,f}^{-f_s}$ component as a function of the short-circuit current, considering the PMSM drive operating at 1200 rpm and rated load, with 3 and 7 short-circuited turns in phase a_1: (a) motoring mode; (b) generating mode.

The analysis of these results reveals a direct proportionality between the amplitude of this component and the short-circuit current, demonstrating a linear correlation with it. Comparing the two faulty cases also demonstrates that the amplitude of this component is also significantly influenced by the number of short-circuited turns, showing a progressive increase accordingly.

Furthermore, in the context of this specific test, it is possible to diagnose faults even when the fault currents are lower than the PMSM rated current ($I_n = 4.8\ A$).

5.4.2 Influence of the Rotor Speed and Load

Figures 5.13 and 5.14 show, in both motoring and generating modes, the evolution of $d^{-f_s}_{\alpha\beta,sc}$ as a function of rotor speed and load, and the evolution of the DOB severity factor defined in (4.5), respectively.

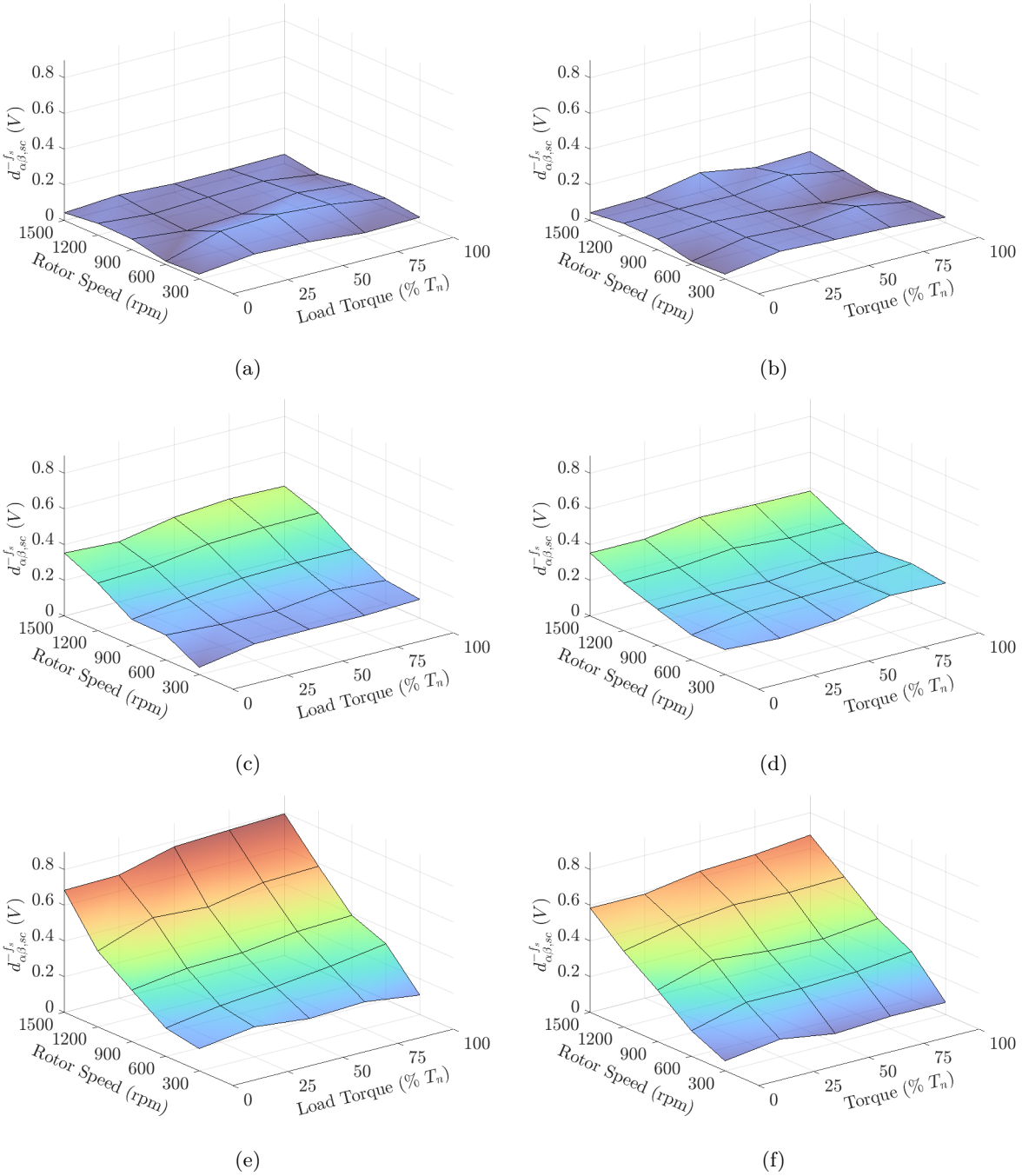

Figure 5.13: Evolution of the experimental $d^{-f_s}_{\alpha\beta,sc}$ as a function of rotor speed and torque: (a) motoring mode with 1 turn; (b) generating mode with 1 turn; (c) motoring mode with 3 turns; (d) generating mode with 3 turns; (e) motoring mode with 7 turns; (f) generating mode with 7 turns.

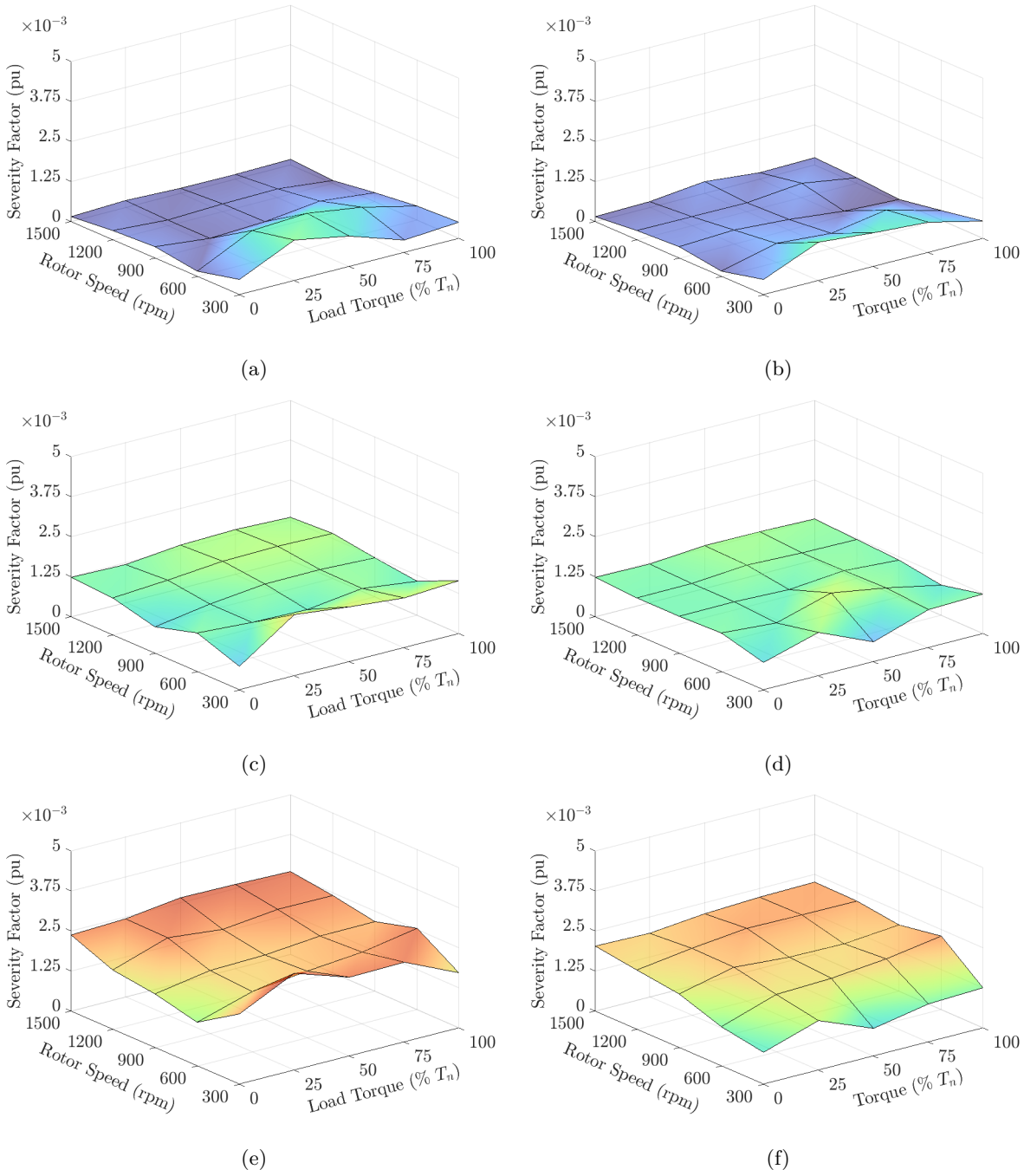

Figure 5.14: Evolution of the DOB severity factor as a function of rotor speed and torque: (a) motoring mode with 1 turn; (b) generating mode with 1 turn; (c) motoring mode with 3 turns; (d) generating mode with 3 turns; (e) motoring mode with 7 turns; (f) generating mode with 7 turns.

The short-circuit current is not only influenced by the impedance of the short-circuited loop but also by the short-circuit voltage, which in turn is proportional to the rotor speed. In light of this, the results presented in Figure 5.13 align with expectations, displaying a clear increase of the short-circuit current with the rotor speed.

In Figure 5.13, the slightly lower $d^{-f_s}_{\alpha\beta,sc}$ value in generating mode compared to motoring

mode, can be attributed to the machine operating mode. By inspecting Table 3.1, when the six-phase PMSM is in generating mode, the voltage at the machine terminals is lower compared to motoring mode. Additionally, these results provide evidence that the load torque has little impact on the amplitude of this component.

The analysis of the evolution of the DOB severity factor in Figure 5.14 reveals that the fault indicator is normalized, thus becoming independent of the rotor speed. Moreover, the severity factor remains minimally affected by the load level.

5.4.3 Robustness Against Deadtime and Parameter Errors

As mentioned previously, in practice the healthy machine may display residual spectral components resulting from various phenomena, such as eccentricities, inherent asymmetries and the influence of the deadtime in the power converters. When spectral components arise from these phenomena, distinguishing between a healthy and faulty machine becomes challenging.

An increase in deadtime from 2.2 μs to 4.4 μs was made in the cRIO control panel in order to verify its impact in the obtained results. The results are shown in Figure 5.15.

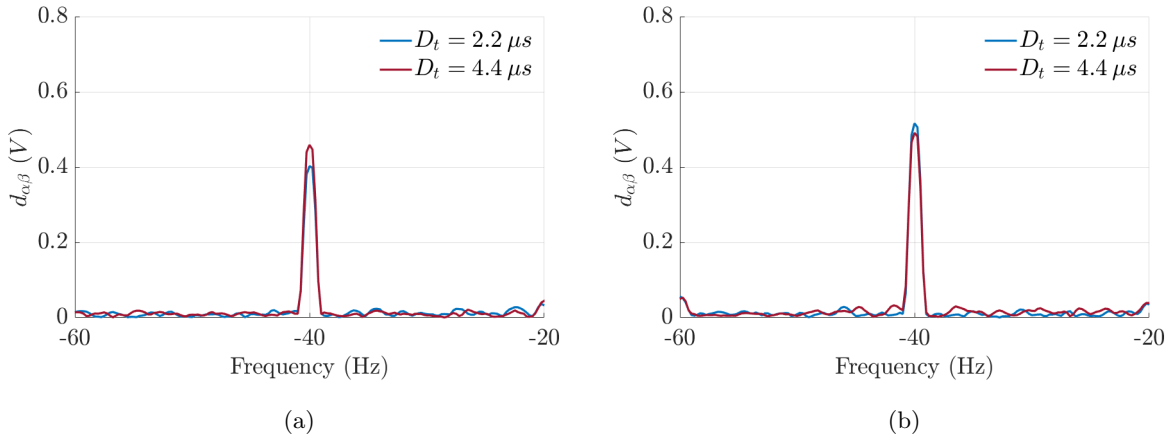

Figure 5.15: Experimental results for $d^{-f_s}_{\alpha\beta,f}$ considering the six-phase PMSM operating at 1200 rpm with a load level of 50%, with 3 short-circuited turns, under different deadtime values: (a) motoring mode; (b) generating mode.

Figure 5.15 shows a small increase in the spectral component at the frequency $-40\,Hz\,(-f_s)$. The DOB compensates the reduced voltage applied to the motor due to the increased deadtime, by increasing its output and reference voltage component at the fundamental frequency. Thus, it becomes clear that deadtime does not impact $d^{-f_s}_{\alpha\beta,f}$ significantly.

To evaluate the behaviour of the DOB output under parameter mismatch errors, different experimental tests were conducted. The parameter errors were introduced only in the control strategy by software in the ControlDesk panel, as seen in Appendix C Figure C.8. The variables

resultant values are defined in the following way:

$$\begin{aligned} R_s = kR_s \cdot R_{s,n}, \quad L_{dq} = kL_{dq} \cdot L_{dq,n}, \\ L_{xy} = kL_{xy} \cdot L_{xy,n}, \quad \psi_{PM1} = k\psi_{PM1} \cdot \psi_{PM1,n} \end{aligned} \tag{5.1}$$

where $\{R_{s,n}, L_{dq,n}, L_{xy,n}, \psi_{PM1,n}\}$ and $\{R_s, L_{dq}, L_{xy}, \psi_{PM1}\}$, are the nominal values of the PMSM parameters and the values considered by the control strategy, respectively.

To validate the robustness against parameter errors, errors of 0.5 and 1.5 were introduced, which is equivalent to 50% and 150% of the PMSM nominal values. Additionally, for the parameter $k\psi_{PM1}$, errors of 0.8 and 1.2 were considered, equivalent to 80% and 120% of the nominal value, respectively.

Figure 5.16 shows the experimental results obtained from these tests in motoring mode.

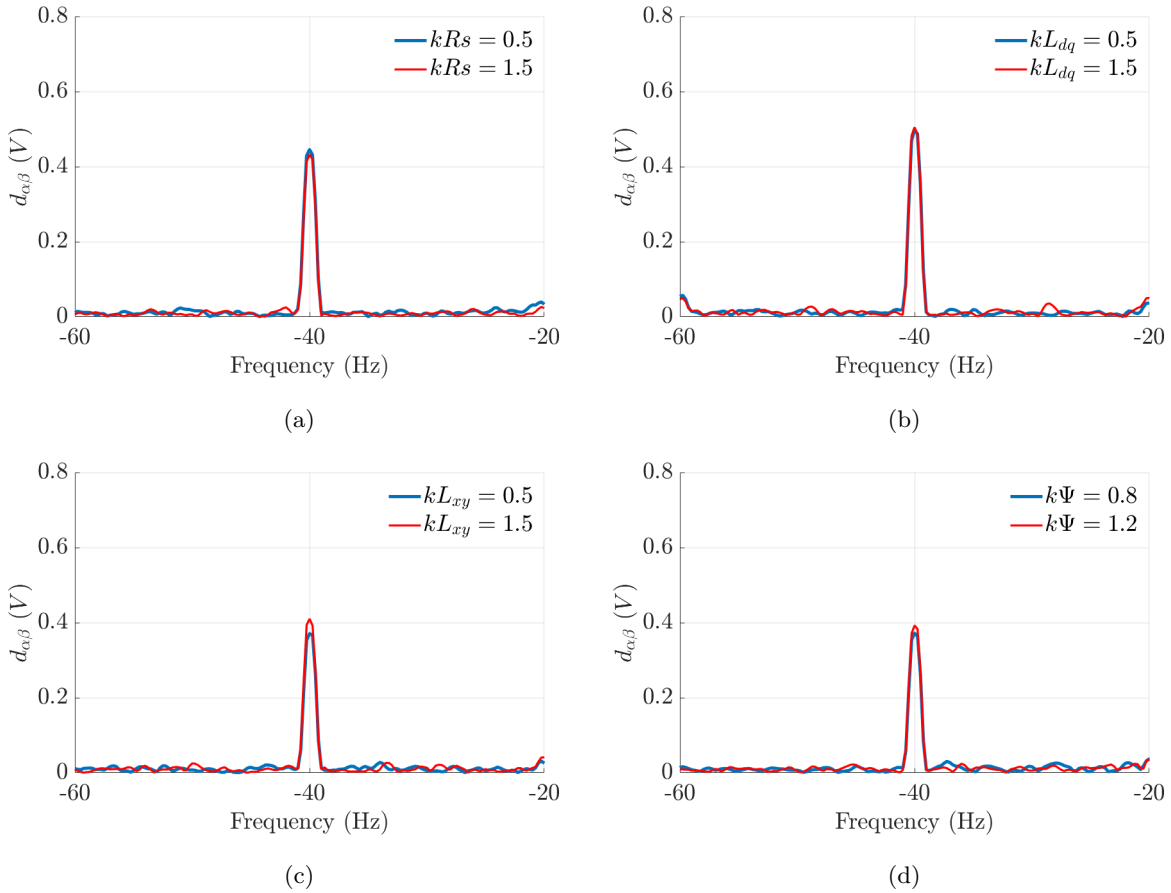

Figure 5.16: Experimental results for $d^{-f_s}_{\alpha\beta,f}$ considering the six-phase PMSM operating at 1200 rpm with a load level of 50% in motoring mode, with 3 short-circuited turns, due to parameter erros in: (a) R_s; (b) L_{dq}; (c) L_{xy}; (d) Ψ_{PM1}.

When subjected to various parameter errors the component $d^{-f_s}_{\alpha\beta,f}$ maintains the same value which validates the robustness against parameter errors.

Figure 5.17 shows the experimental results obtained to the robustness against parameter errors, when the six-phase PMSM is in generating mode.

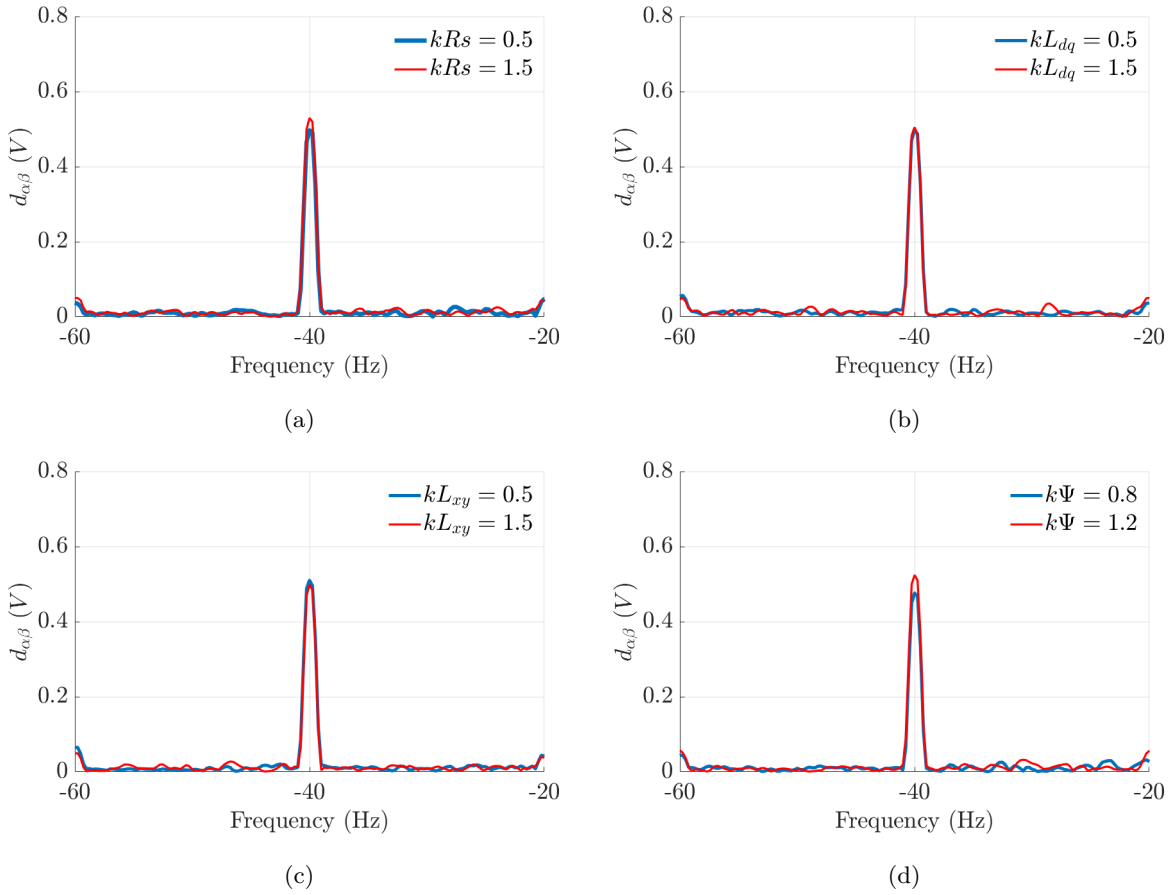

Figure 5.17: Experimental results for $d^{-f_s}_{\alpha\beta,f}$ considering the six-phase PMSM operating at 1200 rpm with a load level of 50% in generating mode, with 3 short-circuited turns, due to parameter erros: (a) R_s; (b) L_{dq}; (c) L_{xy}; (d) Ψ_{PM1}.

From the results obtained in generating mode, the values of $d^{-f_s}_{\alpha\beta,f}$ remain practically the same under parameter errors and the conclusions taken for motoring mode remain the same.

5.4.4 Faulty-Phase Location

The interturn short-circuit creates a negative sequence component at fundamental frequency in $\alpha\beta$ subspace in both DOB output and reference voltages, with the theoretical space vector leaning towards the faulty phase. The faulty phase location is based on the phase analysis of the negative sequence components of the DOB ($\underline{d}^{-f_s}_{\alpha\beta,f}$) and reference voltage ($\underline{u}^{-f_s}_{\alpha\beta,f}$).

Mathematically, a complex space vector can be represented in terms of its positive and negative sequence components. In this context, negative sequence components are complex numbers that rotate clockwise in the complex plane.

The asymmetrical six-phase PMSM under study has a displacement of 30 electrical degrees between each set of three-phase windings. When analyzing the negative sequence component produced by an interturn short-circuit in phase a_2, theoretically, this vector will appear 60º behind, counterclockwise, from the same component with an interturn short-circuit in phase a_1. The following Figure 5.18 presents the previously said.

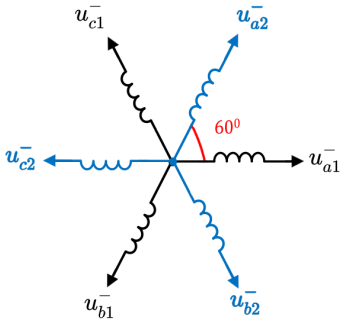

Figure 5.18: Theoretical negative sequence components of spatial vector $\underline{u}_{\alpha\beta}$ in a asymmetrical six-phase PMSM.

To locate the faulty phase using the DOB output, several simulations and experimental results were conducted, both with 7 short-circuited turns. To proceed with the localization not only the amplitude but also the phase of the spatial vector $\underline{d}_{\alpha\beta,f}^{-f_s}$ was taken into account. Figure 5.19 shows the simulation results for the spatial vectors $\underline{d}_{\alpha\beta,f}^{-f_s}$ when the fault is located in different phases.

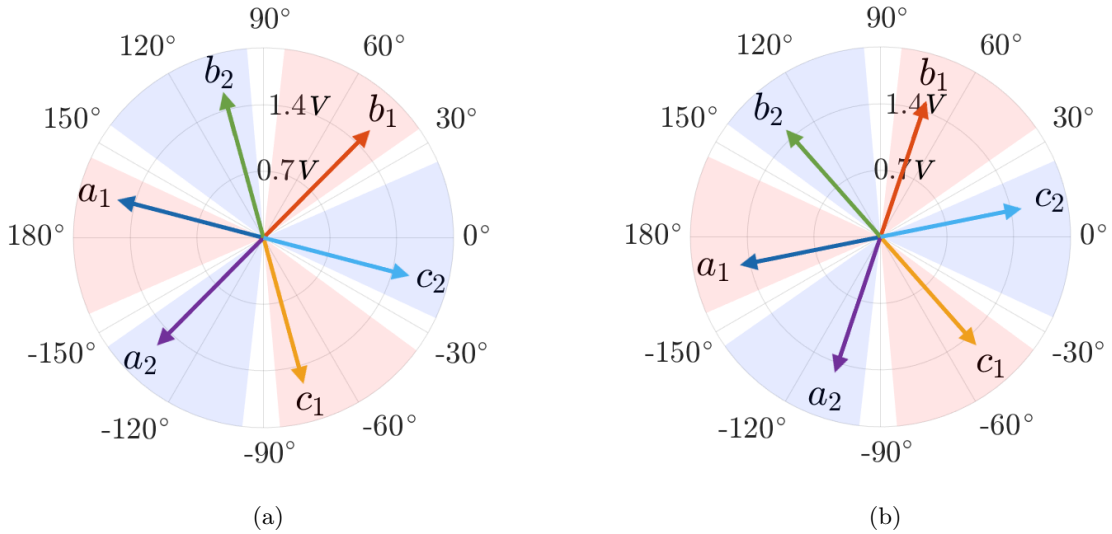

Figure 5.19: Simulation results for $\underline{d}_{\alpha\beta,f}^{-f_s}$ for an interturn short-circuit ($N_{sc} = 7$ and $R_{sc} = 0.5\,\Omega$) in each phase, when the six-phase PMSM operates at 1500 rpm with rated load: (a) motoring mode; (b) generating mode.

Figure 5.19 shows a 60º displacement between two consecutive faulty phases such as phase a_1 and a_2. Since $\underline{d}^{-f_s}_{\alpha\beta,f}$ its a negative sequence component, the sequence of faulty phases space vectors appears in the clockwise direction. Regarding the faulty-phase location it appears that $\underline{d}^{-f_s}_{\alpha\beta,f}$ has a displacement of arround 180º from the axis of the faulty phase. During the investigation of this component, it was observed that the DOB output tends to be in phase opposition with the voltage component. This is evident in the analysis and will be demonstrated when presenting the voltage results. Additionally, Figure 5.20 shows the complex plane representation of $\underline{d}_{\alpha\beta}$ in both healthy and faulty states. Although it is visible an asymmetry in the resultant ellipsis leaning toward the faulty phase, this alone does not permit to take much conclusions on the fault since many factors may contribute to this asymmetry.

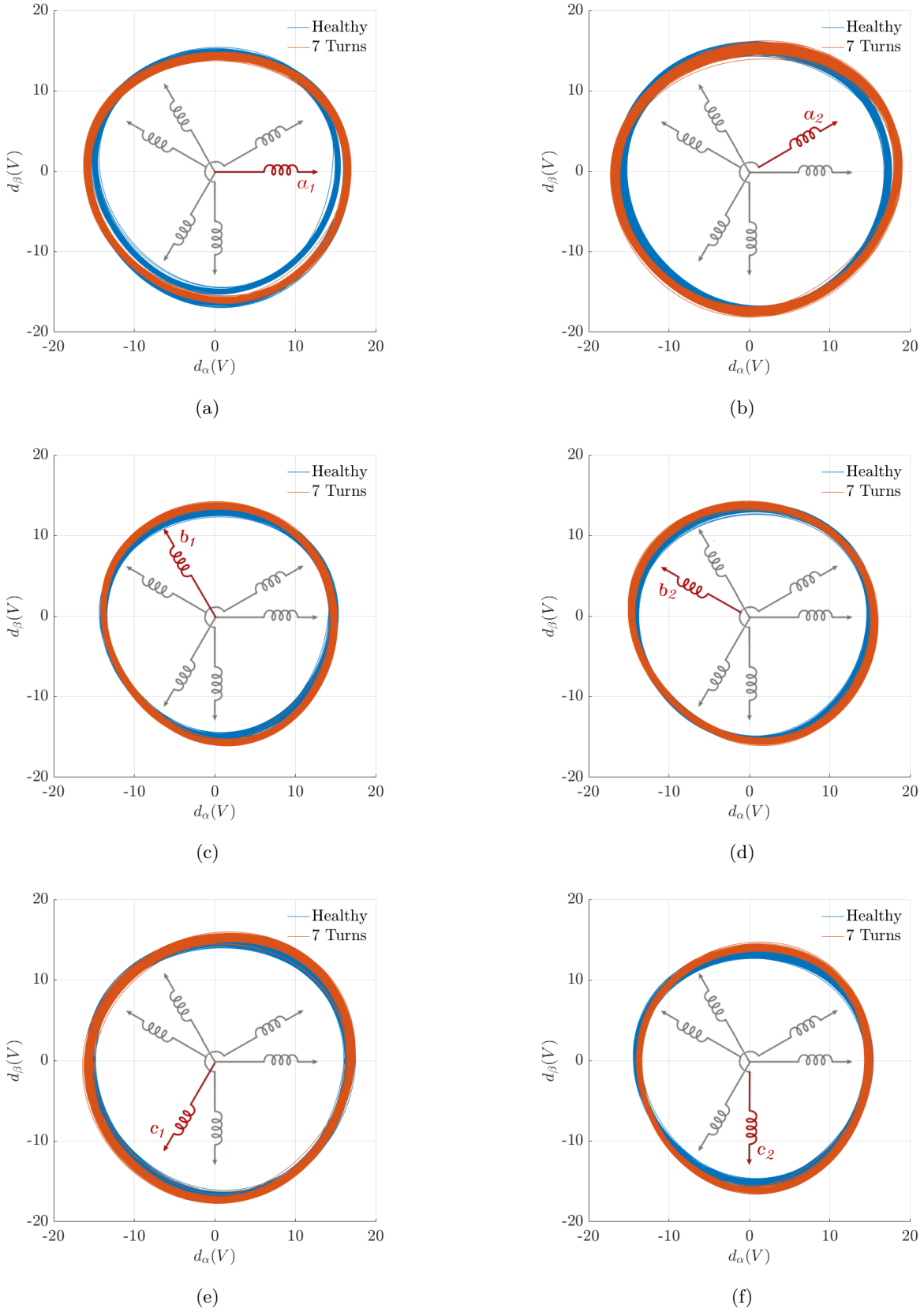

Figure 5.20: Experimental results of filtered $d_\alpha + jd_\beta$ complex representation. Machine with 7 turns in short-circuit at 1200 rpm without load torque: (a) phase a_1; (b) phase a_2; (c) phase b_1; (d) phase b_2; (e) phase c_1; (f) phase c_2.

5.5 Stator Voltage Spectrum Analysis in the $\alpha\beta$ Subspace

This section presents both simulation and experimental results for the stator voltage component, at a frequency of $-f_s$, in the $\alpha\beta$ subspace ($u_{\alpha\beta}^{-f_s}$).

The simulation results presented in Figure 5.21 prove the increase of $u_{\alpha\beta}^{-f_s}$ due to an interturn short-circuit compared to the healthy condition.

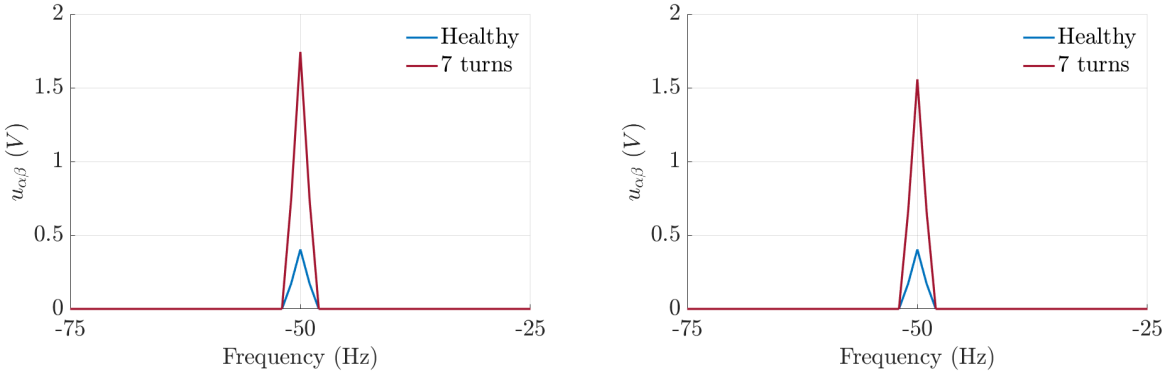

Figure 5.21: Simulation results for $u_{\alpha\beta}^{-f_s}$, considering the PMSM drive operating at 1500 rpm at rated load, with 7 short-circuited turns ($R_{sc} = 0.5\,\Omega$) in phase a_1: (a) motoring mode; (b) generating mode.

The simulation results in Figure 5.21 validate the increase of $u_{\alpha\beta}^{-f_s}$ when the six-phase PMSM is under 7 short-circuited turns. This component is directly related to the interturn short-circuit fault. The lower short-circuit current in generating operation causes $u_{\alpha\beta}^{-f_s}$ to have lower amplitude compared to motoring mode.

5.5.1 Influence of the Short-Circuit Current

Several tests were conducted with both 3 and 7 short-circuited turns in phase a_1, to study the influence of the short-circuit current in $u_{\alpha\beta}^{-f_s}$.

Figure 5.22 presents the evolution of $u_{\alpha\beta}^{-f_s}$ with the fault current.

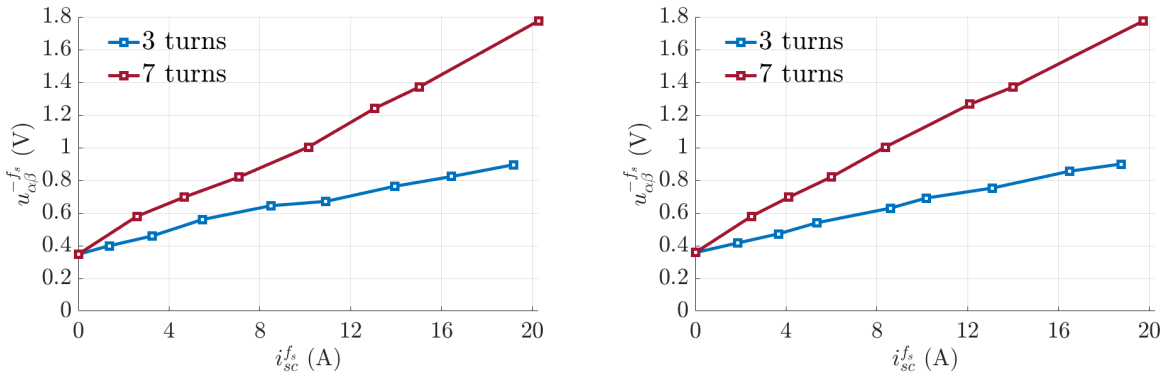

Figure 5.22: Evolution of the experimental $u_{\alpha\beta,f}^{-f_s}$ as a function of the short-circuit current, considering the PMSM drive operating at 1200 rpm, at rated load, with 3 and 7 short-circuited turns in phase a_1: (a) motoring mode; (b) generating mode.

Figure 5.22 reveals a clear increase in $u_{\alpha\beta}^{-f_s}$ amplitude with the increase in the short-circuit current. The amplitude of $u_{\alpha\beta}^{-f_s}$ is also significantly influenced by the number of short-circuited turns, showing a progressive increase accordingly. Furthermore, it is also possible to diagnose this type of fault even when the short-circuit current is lower than the PMSM rated current ($I_n = 4.8\ A$).

Comparing the results of $u_{\alpha\beta}^{-f_s}$ with the ones of $d_{\alpha\beta}^{-f_s}$, in Figure 5.12, it was concluded that $u_{\alpha\beta}^{-f_s}$ has increased amplitude.

5.5.2 Influence of the Rotor Speed and Load

The behavior of $u_{\alpha\beta,sc}^{-f_s}$ as a function of six-phase PMSM load level and rotor speed for different numbers of short-circuited turns is presented in Figure 5.23.

Upon inspecting Figure 5.23 it is evident that this fault indicator is highly dependent on the PMSM rotor speed, while the load level does not have a significant impact. Additionally, as expected, when the six-phase PMSM is under 1 short-circuited turn, $u_{\alpha\beta,sc}^{-f_s}$ exhibits a noticeably smaller amplitude value compared to the results for 3 and 7 short-circuited turns.

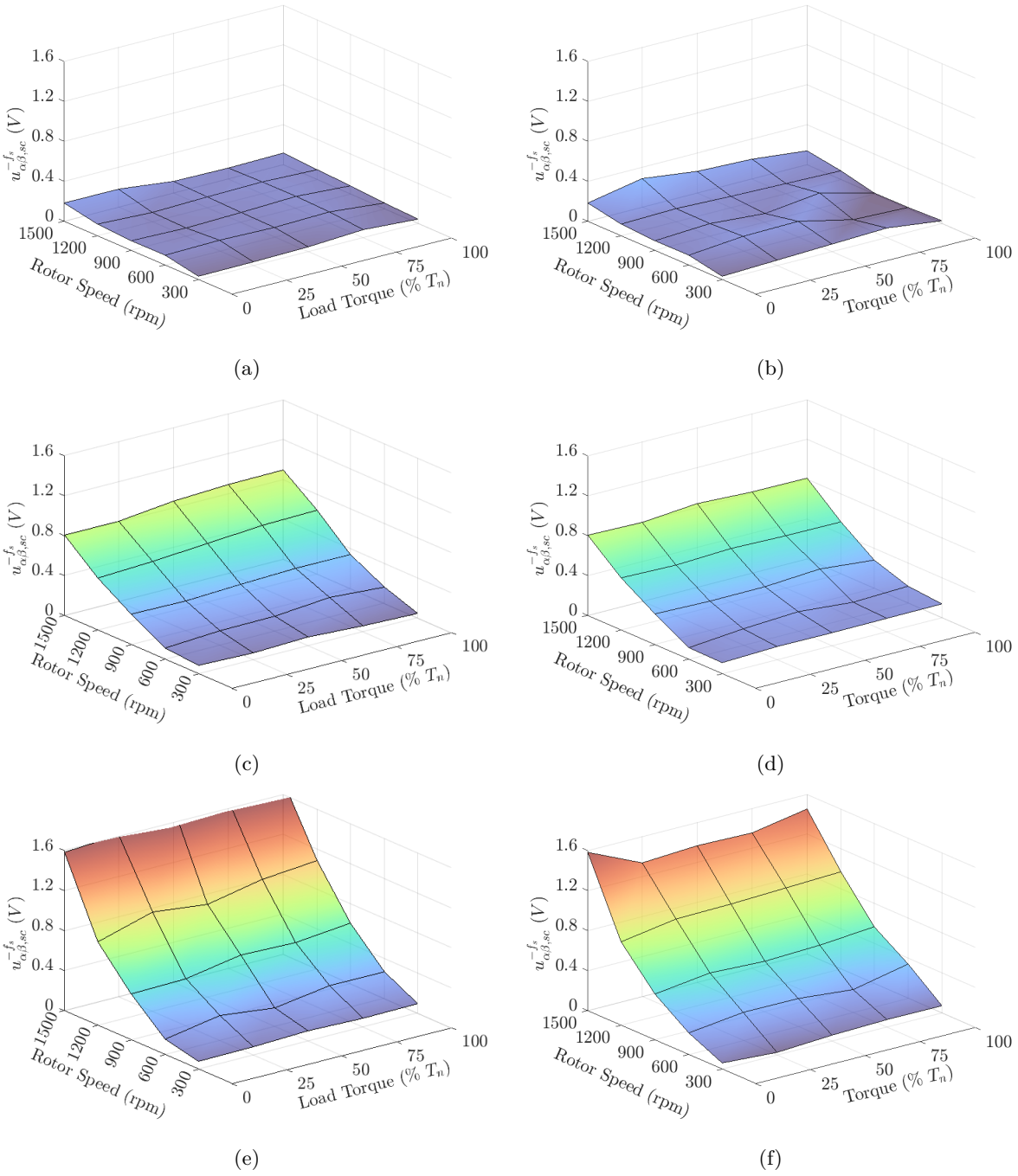

Figure 5.23: Evolution of the experimental $u^{-f_s}_{\alpha\beta,sc}$ as a function of rotor speed and torque: (a) motoring mode with 1 turn; (b) generating mode with 1 turn; (c) motoring mode with 3 turns; (d) generating mode with 3 turns; (e) motoring mode with 7 turns; (f) generating mode with 7 turns.

The evolution of the voltage severity factor, defined in (4.8), for different speed and load levels is presented in Figure 5.24.

Figure 5.24 shows that this indicator becomes less dependent on the PMSM rotor speed. The results match the expected ones since the reference voltage is mainly proportional to the PMSM rotor speed.

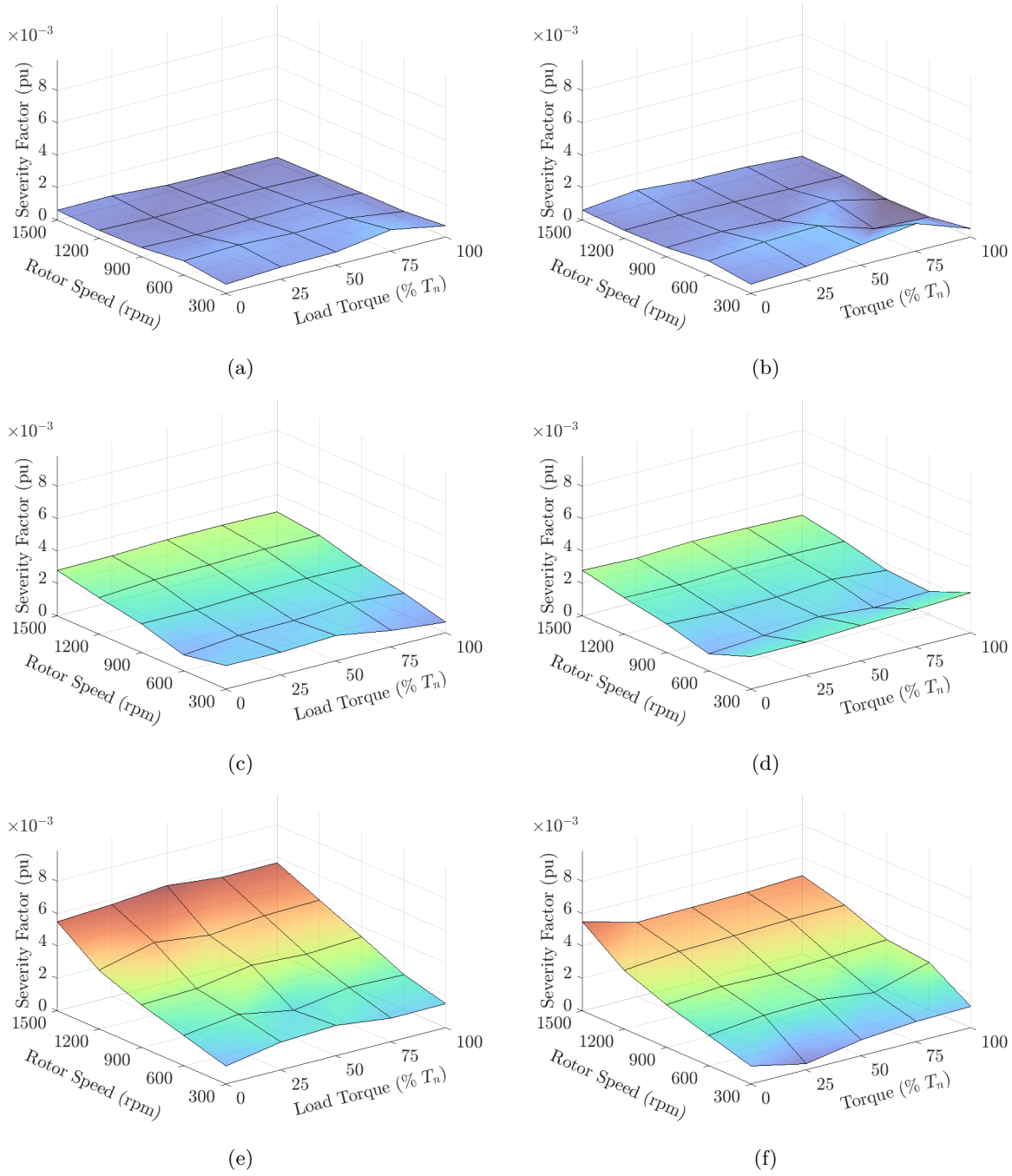

Figure 5.24: Evolution of the voltage severity factor as a function of rotor speed and torque: (a) motoring mode with 1 turn; (b) generating mode with 1 turn; (c) motoring mode with 3 turns; (d) generating mode with 3 turns; (e) motoring mode with 7 turns; (f) generating mode with 7 turns.

5.5.3 Robustness Against Deadtime and Parameter Errors

The same way as in $d_{\alpha\beta}^{-fs}$, Figure 5.25 presents the results obtained for $u_{\alpha\beta}^{-fs}$ when the six-phase PMSM is subjected to different deadtime values.

Figures 5.26 and 5.27 present the experimental results obtained for different parameter errors under motoring and generating operation, respectively.

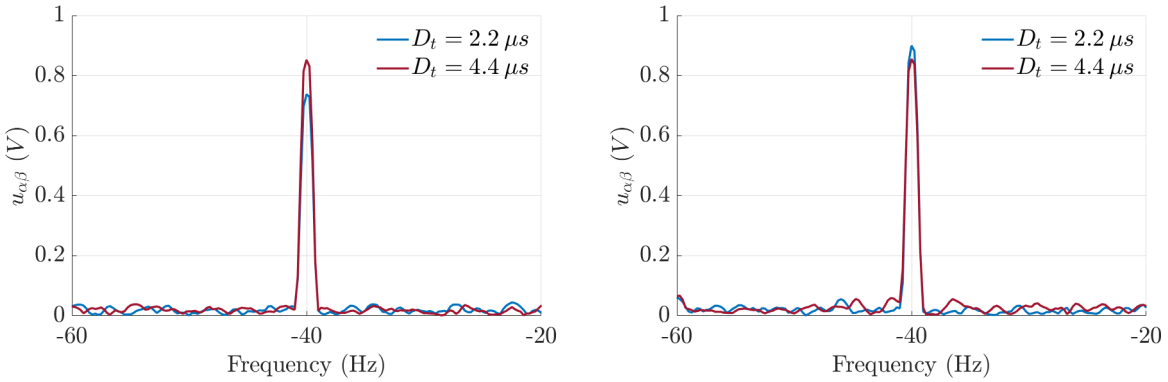

Figure 5.25: Experimental results for $u_{\alpha\beta,f}^{-f_s}$ considering the six-phase PMSM operating at 1200 rpm with a load level of 50%, with 3 short-circuited turns, under different deadtime values: (a) motoring mode; (b) generating mode.

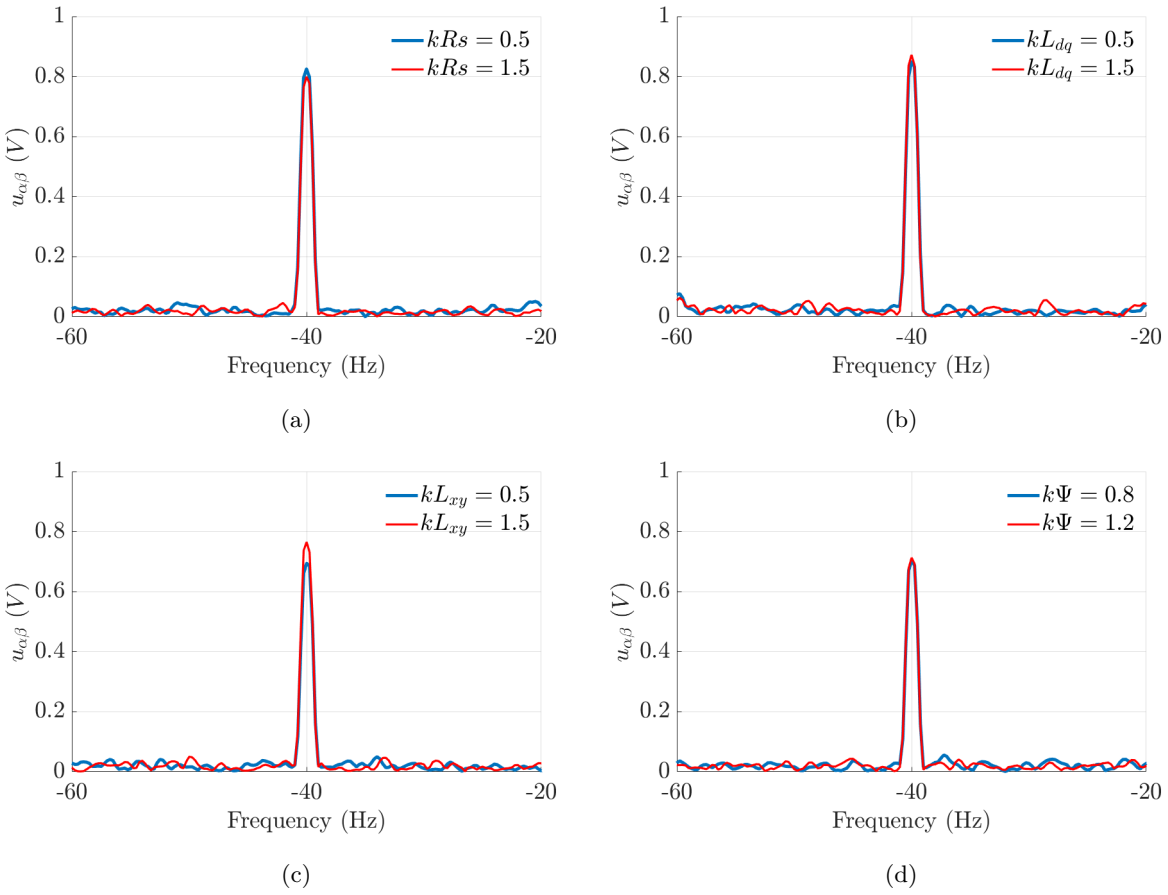

Figure 5.26: Experimental results for $u_{\alpha\beta,f}^{-f_s}$ considering the six-phase PMSM operating at 1200 rpm with a load level of 50% in motoring mode, with 3 short-circuited turns, due to parameter erros in: (a) R_s; (b) L_{dq}; (c) L_{xy}; (d) Ψ_{PM1}.

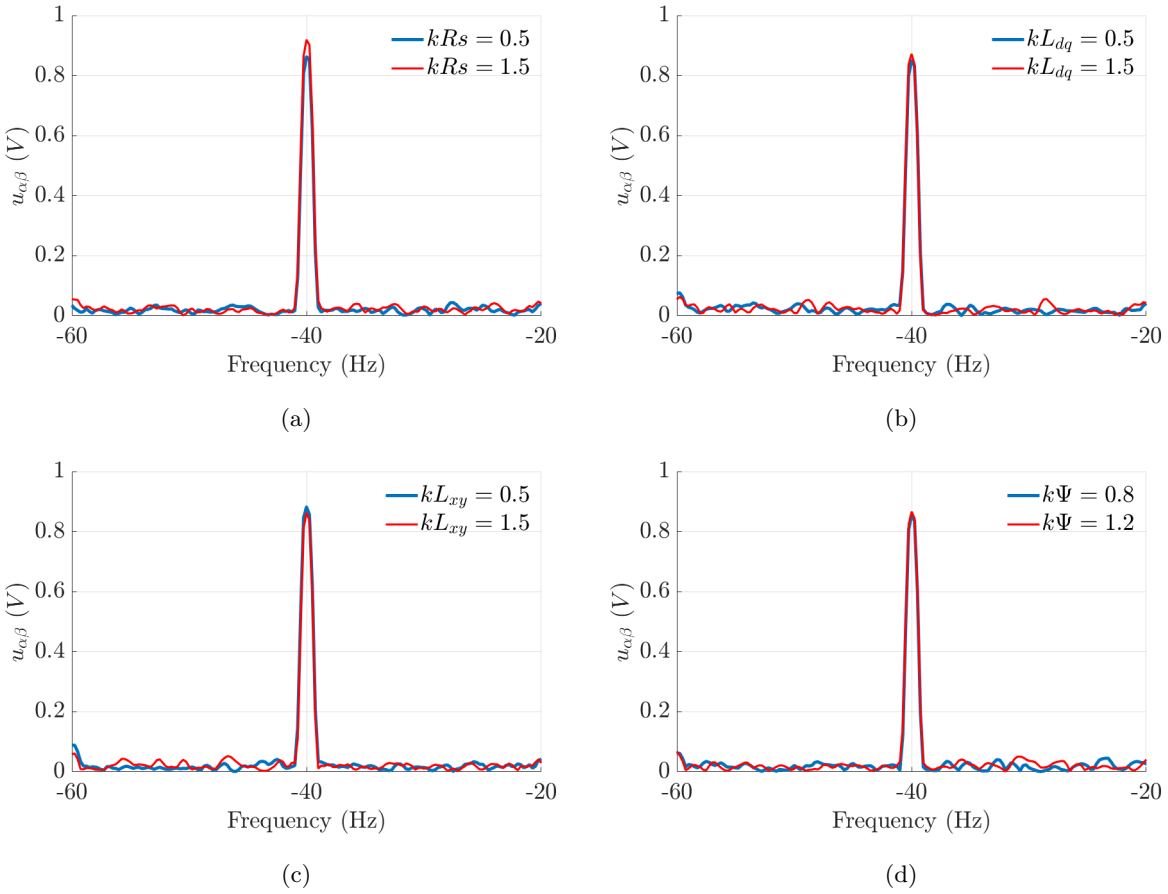

Figure 5.27: Experimental results for $u_{\alpha\beta,f}^{-f_s}$ considering the six-phase PMSM operating at 1200 rpm with a load level of 50% in generating mode, with 3 short-circuited turns, due to parameter erros in: (a) R_s; (b) L_{dq}; (c) L_{xy}; (d) Ψ_{PM1}.

The presented results are very similar to the $d_{\alpha\beta}^{-f_s}$ ones. The influence of deadtime and parameter errors in $u_{\alpha\beta}^{-f_s}$ is insignificant, which also validates the robustness of this component under parameter mismatch errors.

5.5.4 Faulty-Phase Location

The spatial vector $\underline{u}_{\alpha\beta,f}^{-f_s}$ changes its location in the complex plan according to the faulty phase.

Figure 5.28 exhibits the space vectors of $\underline{u}_{\alpha\beta,f}^{-f_s}$ obtained by the cosimulation study for each one of the six faulty phases of the PMSM.

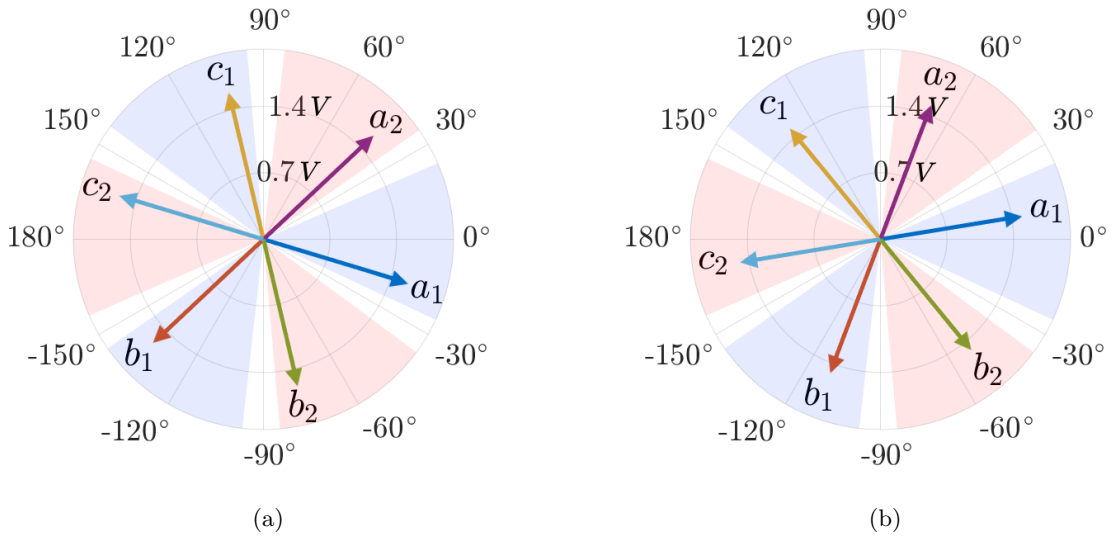

Figure 5.28: Simulation results for $\underline{u}_{\alpha\beta,f}^{-f_s}$ for an interturn short-circuit ($N_{sc} = 7$ and $R_{sc} = 0.5\Omega$) in each phase of the six-phase PMSM when it operates at 1500 rpm with rated load: (a) motoring mode; (b) generating mode.

The simulation results validate that the interturn short-circuit creates a negative sequence component in the reference voltages in the direction of the faulty phase, enabling the location of the fault. This component is mainly influenced by the PMSM operating mode and load level. When operating at rated load, in motoring mode, the vectors shift 15º in the clockwise direction, while in the generating mode, they shift in the counterclockwise direction.

In the simulation environment, the machine is perfectly balanced and exhibits no asymmetries. Therefore, there are no negative sequence components that impact the fault indicator. However, in the experimental environment, every machine has some residual asymmetry due to different factors, as previously discussed. To achieve a more reliable fault location the component decoupled from residual asymmetries was studied in the experimental test. Figures 5.29a and 5.29b present the experimental results for the component decoupled from residual asymmetries.

The experimental results validate the simulation results presented, however, as expected, both amplitude and phases do not follow so perfectly the simulation due to the PMSM inherent residual asymmetries.

To provide a clearer representation of the faulty zones relative to the damaged phase, a phase compensation was implemented based on the simulation results. With a load level of 100% in motoring mode, the faulty zones shift -15º, while in the motoring mode they shift 15º. Figures 5.29c and 5.29d illustrate this compensation.

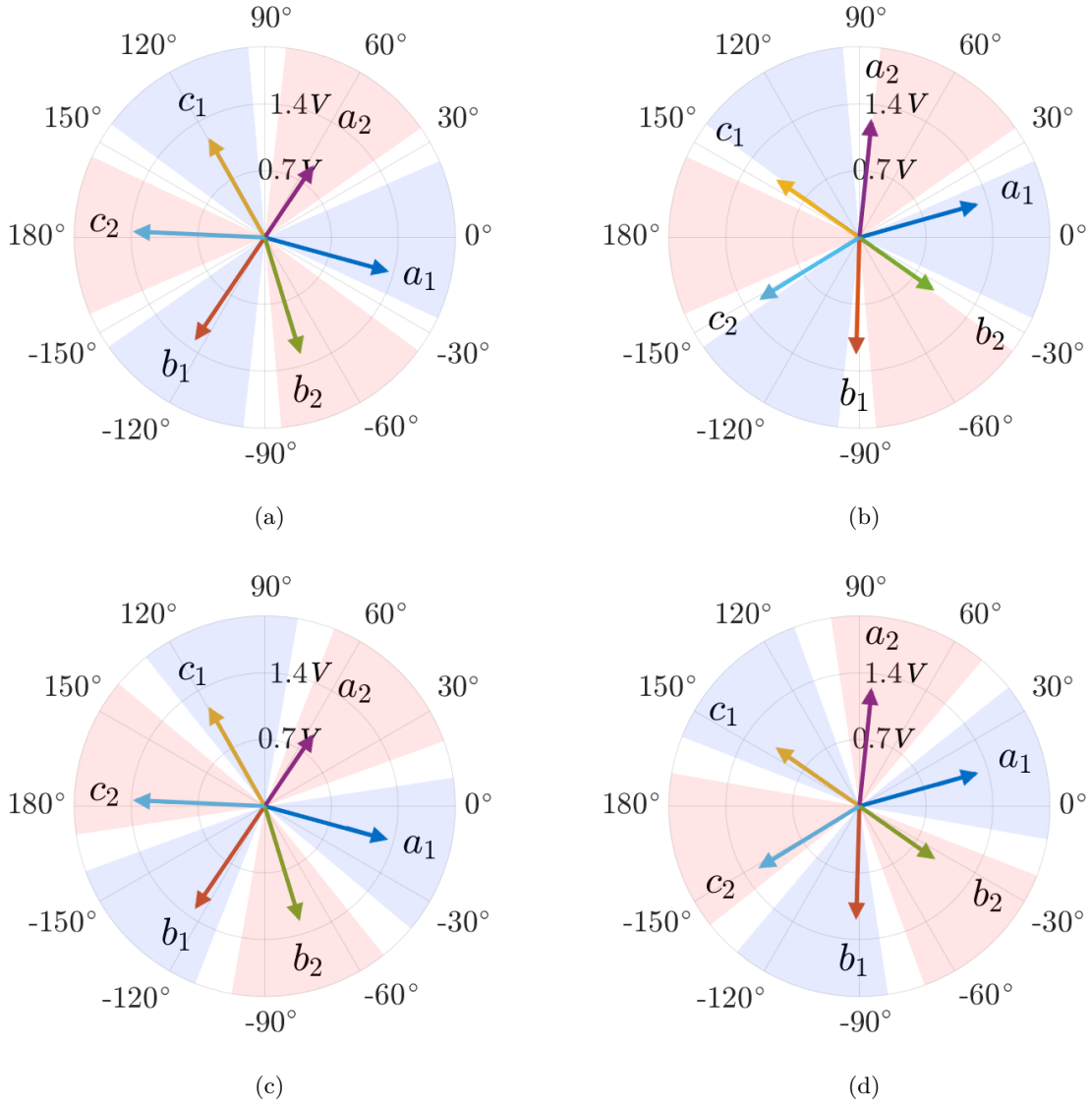

Figure 5.29: Experimental results for $\underline{u}^{-f_s}_{\alpha\beta,sc}$ for an interturn short-circuit ($N_{sc} = 7$ and $R_{sc} = 0.4\Omega$) in each phase when the six-phase PMSM operates at 1200 rpm with rated load: (a) motoring mode; (b) generating mode; (c) motoring mode with faulty zone compensation; (d) generating mode with faulty zone compensation.

The compensation of the faulty zones based on the operating mode of the six-phase PMSM improves fault detection and provides potential for future algorithms where the load angle could be calculated and compensated. However, this is beyond the scope of this dissertation.

Upon comparing the results obtained for the faulty-phase location using $\underline{d}^{-f_s}_{\alpha\beta,f}$ and $\underline{u}^{-f_s}_{\alpha\beta,f}$, it was observed that the phase of $\underline{d}^{-f_s}_{\alpha\beta,f}$ tends to oppose that of $\underline{u}^{-f_s}_{\alpha\beta,f}$, leading to an incorrect identification of the faulty-phase. To further investigate the amplitude and phase difference between $\underline{d}^{-f_s}_{\alpha\beta,f}$ and $\underline{u}^{-f_s}_{\alpha\beta,f}$, the Tables 5.1 and 5.2 were developed for analysis in both motoring and generating modes, respectively. The phase shift, denoted as the shortest phase between

each component, is expressed as: $\angle \underline{u}^{-f_s}_{\alpha\beta,f} - \angle \underline{d}^{-f_s}_{\alpha\beta,f}$.

Table 5.1: Simulation and experimental results for the amplitude and phase of $\underline{d}^{-f_s}_{\alpha\beta,f}$ and $\underline{u}^{-f_s}_{\alpha\beta,f}$ for an interturn short-circuit (Nsc = 7) in each phase when the six-phase PMSM operates in motoring mode at 1200 rpm with rated load.

Type of data	Faulty phase	$\lvert\underline{d}^{-f_s}_{\alpha\beta,f}\rvert$	$\angle\underline{d}^{-f_s}_{\alpha\beta,f}$	$\lvert\underline{u}^{-f_s}_{\alpha\beta,f}\rvert$	$\angle\underline{u}^{-f_s}_{\alpha\beta,f}$	$\angle\underline{u}^{-f_s}_{\alpha\beta,f} - \angle\underline{d}^{-f_s}_{\alpha\beta,f}$
Simulation	a_1	$1.00\,V$	$166°$	$1.00\,V$	$-16°$	**178°**
Experimental	a_1	$0.90\,V$	$-144°$	$1.68\,V$	$-22°$	**122°**
	b_1	$0.71\,V$	$130°$	$1.38\,V$	$-107°$	**123°**
	c_1	$0.44\,V$	$-11°$	$0.76\,V$	$113°$	**124°**
	a_2	$0.51\,V$	$-91°$	$0.92\,V$	$29°$	**119°**
	b_2	$0.84\,V$	$-175°$	$1.59\,V$	$-64°$	**121°**
	c_2	$0.57\,V$	$67°$	$1.07\,V$	$-169°$	**125°**

Table 5.2: Simulation and experimental results for the amplitude and phase of $\underline{d}^{-f_s}_{\alpha\beta,f}$ and $\underline{u}^{-f_s}_{\alpha\beta,f}$ for an interturn short-circuit (Nsc = 7) in each phase when the six-phase PMSM operates in generating mode at 1200 rpm with rated load.

Type of data	Faulty phase	$\lvert\underline{d}^{-f_s}_{\alpha\beta,f}\rvert$	$\angle\underline{d}^{-f_s}_{\alpha\beta,f}$	$\lvert\underline{u}^{-f_s}_{\alpha\beta,f}\rvert$	$\angle\underline{u}^{-f_s}_{\alpha\beta,f}$	$\angle\underline{u}^{-f_s}_{\alpha\beta,f} - \angle\underline{d}^{-f_s}_{\alpha\beta,f}$
Simulation	a_1	$0.94\,V$	$-168°$	$0.94\,V$	$10°$	**178°**
Experimental	a_1	$0.85\,V$	$-101°$	$1.58\,V$	$22°$	**122°**
	b_1	$0.48\,V$	$164°$	$0.93\,V$	$-75°$	**120°**
	c_1	$0.55\,V$	$1°$	$1.00\,V$	$125°$	**124°**
	a_2	$0.85\,V$	$-49°$	$1.53\,V$	$74°$	**122°**
	b_2	$0.55\,V$	$-140°$	$1.02\,V$	$-19°$	**121°**
	c_2	$0.45\,V$	$82°$	$0.87\,V$	$-153°$	**124°**

The presented results show that in the experimental data, the phase shift between $\underline{d}^{-f_s}_{\alpha\beta,f}$ and $\underline{u}^{-f_s}_{\alpha\beta,f}$ consistently hovers around 120º, in both modes of operation. In the cosimulation data the phase shift between these components is consistently 178º degrees. Comparing the cosimulation alongside the experimental data, disparities emerge, particularly in the phase and amplitude of $\underline{d}^{-f_s}_{\alpha\beta,f}$. Notably, the experimental data exhibits a distinct variation in the amplitudes of $d^{-f_s}_{\alpha\beta,f}$ and $u^{-f_s}_{\alpha\beta,f}$, whereas these differences are not observed in the cosimulation results.

5.6 Complex Apparent Power Spectrum Analysis in the dq Subspace

This section presents both simulation and experimental results for the stator complex apparent power component, at $-2f_s$ in the dq subspace (s_{dq}^{-2}).

The cosimulation results presented in Figure 5.30 show the increase of s_{dq}^{-2} when the six-phase PMSM is under 7 short-circuited turns.

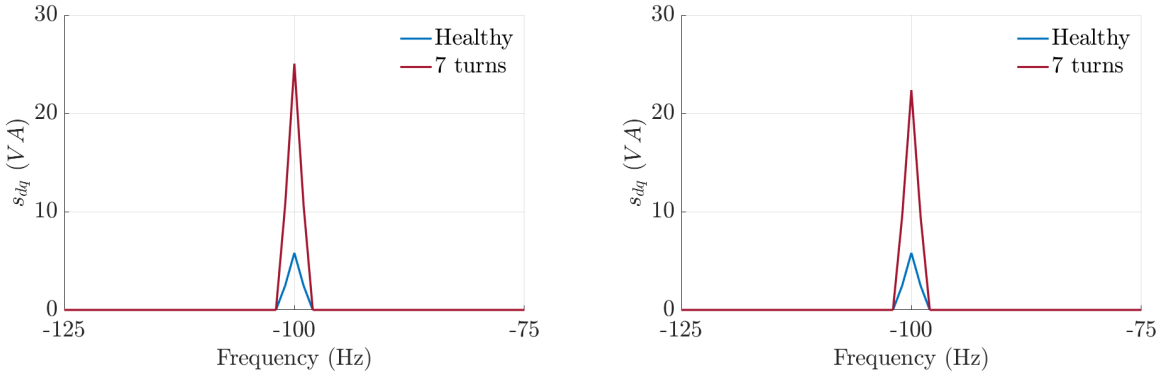

Figure 5.30: Simulation results for the s_{dq}^{-2}, considering the PMSM drive operating at 1500 rpm at rated load with 7 short-circuited turns ($R_{sc} = 0.5\,\Omega$) in phase a_1: (a) motoring mode; (b) generating mode.

Like the previous methods, this component increase is bigger when the six-phase PMSM operates as a motor.

Figure 5.31 shows the evolution of s_{dq}^{-2} when the six-phase PMSM operates with 7 turns in short-circuit at different rotor speeds.

The increment of s_{dq}^{-2} is directly associated with the interturn short-circuit. As seen in Figure 5.31, the amplitude of this component at lower speeds, such as 300 rpm, exposes constraints in fault diagnosis. At 600 rpm, fault diagnosis becomes feasible in certain instances but could still go undetected at times. Beyond 600 rpm, the increase in the amplitude of this component is evident.

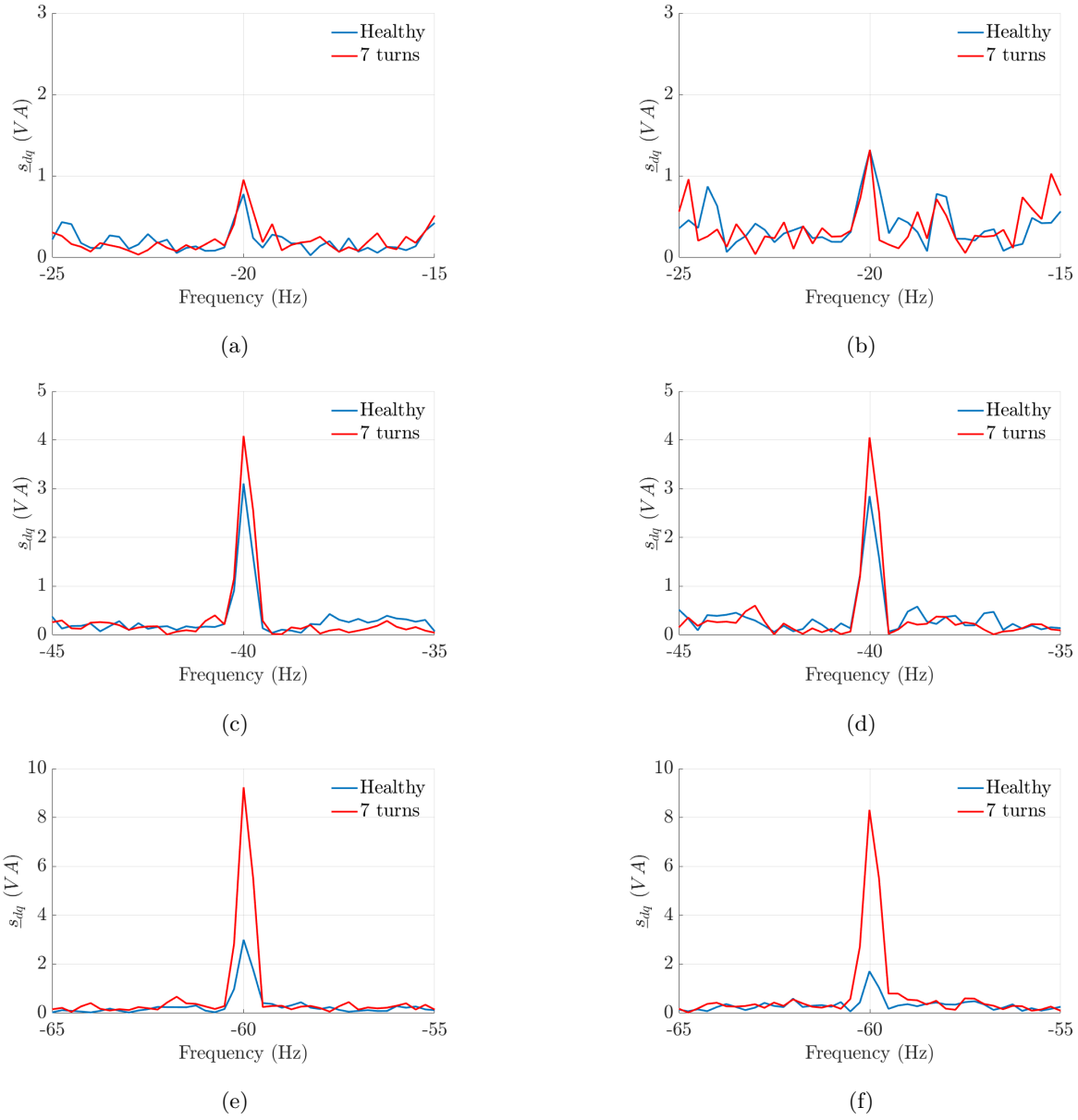

Figure 5.31: Experimental results for s_{dq}^{-2} with the PMSM operating with 7 short-circuited turns in phase a_1 at rated load at: (a) 300 rpm motor; (b) 300 rpm generator; (c) 600 rpm motor; (d) 600 rpm generator; (e) 900 rpm motor; (f) 900 rpm generator.

Figure 5.32 shows the evolution of the stator complex power severity factor, defined in 4.12, for different operating conditions.

The severity factor increases with both the rotor speed and the load torque. As expected when the six-phase PMSM is in motoring operation, the severity factor exhibits a more noticeable increase compared to generating operation.

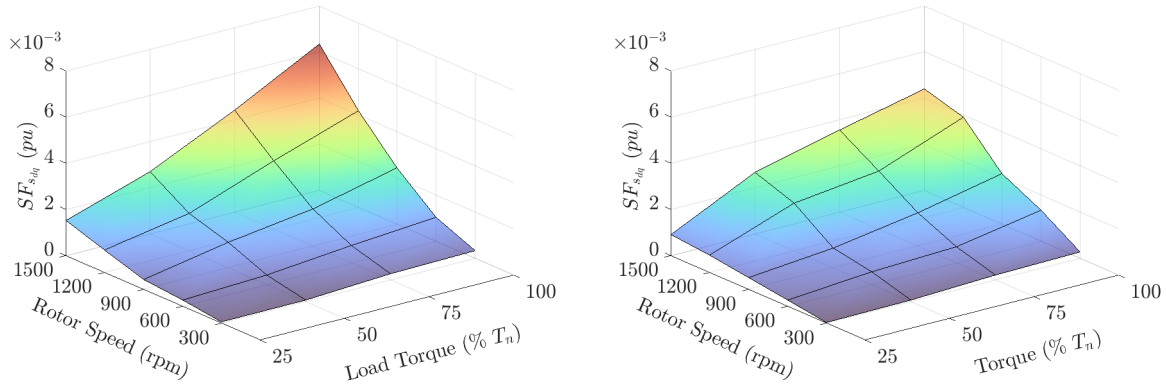

Figure 5.32: Evolution of the stator complex power severity factor as a function of rotor speed and torque with 7 turns in short-circuit: (a) motoring mode; (b) generating mode;

5.7 Comparison of the Diagnostic Methods

This section presents a comprehensive comparison of different diagnostic methods employed in the identification and detection of interturn short-circuits in six-phase PMSMs. The objective is to assess the effectiveness, accuracy and applicability of these methods in the diagnosis of interturn short-circuits. By evaluating their strengths and limitations, this research aims to provide valuable insights into the optimal diagnostic approach for identifying interturn short-circuits in six-phase PMSMs.

The $\underline{d}^{-f_s}_{\alpha\beta,f}$, and $\underline{u}^{-f_s}_{\alpha\beta,f}$ methods, although very similar, reveal advantages over each other in certain aspects. Both methods proved to be robust even in the presence of deadtime and parameter mismatch errors. Regarding fault detection, both methods exhibit a significant increase in the amplitude of the faulty component of the method and respective severity factor. In the experimental environment, the increase of $u^{-f_s}_{\alpha\beta,f}$ was bigger than in $d^{-f_s}_{\alpha\beta,f}$. The DOB output method has the advantage of a much cleaner spectrum enabling the fault diagnosis.

During the process of fault location, the method using $u^{-f_s}_{\alpha\beta,f}$ provides a correct fault location as proven in both simulation and experimental results. The method using the DOB has a considerable phase shift in both simulation and experimental results, as explained before, providing incorrect fault location.

The proposed fault location methods limitation lies in requiring an encoder in the PMSM drive, which restricts the applicability of these methods to drives with encoder.

Regarding the stator complex power method, although the method was exclusively applied to the PMSM operating with 7 short-circuited turns, it becomes evident that this approach is comparatively less effective than its precursors. The previous methods exhibited seamless

detection of 7 short-circuited turns, unlike this one which encounters challenges, particularly at medium and low speeds.

Despite its infrequent occurrence, this method proves inadequate in diagnosing issues when the PMSM operates without a load, while also showing substantial variation in the severity factor according to the load level of the six-phase PMSM.

Overall, the presented methods enable a clear fault diagnosis at medium/high rotor speeds. Difficulties arrise when trying to diagnose the most incipient fault cases which, is one turn in short-circuit, especially at low/medium rotor speeds.

The following Table 5.3 evaluates each method regarding the interturn short-circuit detection and location capabilities. The meaning of "+/-" reveals that the method has limitations either in the detection or location of the fault at that speed.

Table 5.3: Comparision between the presented diagnostic methods considering 7 turns in short-circuit.

Method	Detection			Location
	High speed	Medium speed	Low speed	
$d_{\alpha\beta}^{-f_s}$	Yes	Yes	+/-	+/-
$u_{\alpha\beta}^{-f_s}$	Yes	Yes	+/-	Yes
s_{dq}^{-2}	Yes	+/-	No	No

6 Conclusion and Future Work

6.1 Conclusion

In this dissertation, three fault diagnosis methods were proposed and investigated for six-phase PMSMs. Through validation using both 2D cosimulation models and experimental data, each method was evaluated for its effectiveness in the diagnosis of interturn short-circuit faults.

The findings from this research reveal the capability of each method in accurately detecting interturn short-circuit faults with ease across medium to high rotor speeds. Notably, two of the presented methods also demonstrated the potential to locate the faulty-phase, enhancing their diagnostic accuracy.

This dissertation contributes substantially to the field of fault diagnosis studies. It not only demonstrates the effectiveness of these methods but also highlights their limitations, particularly in scenarios involving lower speeds and small or incipient fault severities, such as a single turn fault.

Among the presented methods, the approach based on the reference voltages emerges as the most reliable overall. This method, previously explored in literature, was validated for this six-phase PMSM through our investigation, while showcasing the potential for fault location, an aspect that lacks in literature.

Furthermore, the DOB output signal method displays diagnostic capabilities comparable to the reference voltages method with an overall cleaner spectrum but stays behind in fault location. This finding opens the door for future explorations of fault diagnosis using different types of observers.

On the other hand, the stator complex power method exhibited relatively diminished efficacy compared to the other diagnostic methods. It showed limitations, particularly in medium-speed scenarios even to diagnose seven short-circuited turns.

In conclusion, this dissertation expands the knowledge of fault diagnosis in six-phase PMSMs. The research solidifies the credibility of existing diagnostic methodologies while introducing in-

novative strategies that broaden the options for reliable interturn short-circuit fault diagnosis. While certain limitations have been identified, this dissertation opens the way for further investigations and advancements in fault diagnosis methods in multiphase machines.

6.2 Future Work

The research work made in this dissertation leaves space for several future research topics such as:

- Validate the diagnostic methods in other electric drives with observers implemented.
- Validate the methods for the same PMSM drive under a 1N configuration.
- Validate the phase location to less short circuited-turns such as 1 and 3 turns.
- Extend the phase location to other six-phase PMSM configurations such as the dual three-phase and symmetrical ones.
- Extend the methods to other multiphase machines such as five-phase, nine-phase, or other topologies.
- Develop a load angle compensation algorithm for precise faulty phase location using reference voltages.
- Extend the fault location for drives without an encoder.

References

[1] A. Akrad, M. Hilairet, and D. Diallo, "Design of a fault-tolerant controller based on observers for a pmsm drive," *IEEE Transactions on Industrial Electronics*, vol. 58, no. 4, pp. 1416–1427, 2011.

[2] V. Yaramasu, A. Dekka, M. J. Durán, S. Kouro, and B. Wu, "Pmsg-based wind energy conversion systems: survey on power converters and controls," *IET Electric Power Applications*, vol. 11, no. 6, pp. 956–968, 2017.

[3] M. Duran, E. Levi, and F. Barrero, *Multiphase Electric Drives. Introduction.*, pp. 1–26. Hoboken, NJ, USA: John Wiley and Sons, Inc., 2017.

[4] F. Barrero and M. J. Duran, "Recent advances in the design, modeling, and control of multiphase machines—part i," *IEEE Transactions on Industrial Electronics*, vol. 63, no. 1, pp. 449–458, 2016.

[5] T. M. Jahns, "Improved reliability in solid-state ac drives by means of multiple independent phase drive units," *IEEE Transactions on Industry Applications*, vol. IA-16, no. 3, pp. 321–331, 1980.

[6] H. Toliyat, L. Xu, and T. Lipo, "A five-phase reluctance motor with high specific torque," *IEEE Transactions on Industry Applications*, vol. 28, no. 3, pp. 659–667, 1992.

[7] E. Levi, "Advances in converter control and innovative exploitation of additional degrees of freedom for multiphase machines," *IEEE Transactions on Industrial Electronics*, vol. 63, no. 1, pp. 433–448, 2016.

[8] A. Salem and M. Narimani, "A review on multiphase drives for automotive traction applications," *IEEE Transactions on Transportation Electrification*, vol. 5, no. 4, pp. 1329–1348, 2019.

[9] W. Cao, B. C. Mecrow, G. J. Atkinson, J. W. Bennett, and D. J. Atkinson, "Overview of electric motor technologies used for more electric aircraft (mea)," *IEEE Transactions on Industrial Electronics*, vol. 59, no. 9, pp. 3523–3531, 2012.

[10] A. Damiano, I. Marongiu, A. Monni, and M. Porru, "Design of a 10 mw multi-phase pm synchronous generator for direct-drive wind turbines," in *IECON 2013 - 39th Annual Conference of the IEEE Industrial Electronics Society*, pp. 5266–5270, 2013.

[11] P. F. Gonçalves, S. M. Cruz, and A. M. Mendes, "Design of a six-phase asymmetrical permanent magnet synchronous generator for wind energy applications," *The Journal of Engineering*, vol. 2019, no. 17, pp. 4532–4536, 2019.

[12] P. F. Gonçalves, S. M. Cruz, and A. M. S. Mendes, "Disturbance observer based predictive current control of six-phase permanent magnet synchronous machines for the mitigation of steady-state errors and current harmonics," *IEEE Transactions on Industrial Electronics*, vol. 69, no. 1, pp. 130–140, 2022.

[13] Y. Qi, E. Bostanci, V. Gurusamy, and B. Akin, "A comprehensive analysis of short-circuit current behavior in pmsm interturn short-circuit faults," *IEEE Transactions on Power Electronics*, vol. 33, no. 12, pp. 10784–10793, 2018.

[14] T. Orlowska-Kowalska, M. Wolkiewicz, P. Pietrzak, M. Skowron, P. Ewert, G. Tarchala, M. Krzysztofiak, and C. T. Kowalski, "Fault diagnosis and fault-tolerant control of pmsm drives–state of the art and future challenges," *IEEE Access*, vol. 10, pp. 59979–60024, 2022.

[15] M. Cheng, J. Hang, and J. Zhang, "Overview of fault diagnosis theory and method for permanent magnet machine," *Chinese Journal of Electrical Engineering*, vol. 1, no. 1, pp. 21–36, 2015.

[16] M. Zafarani, E. Bostanci, Y. Qi, T. Goktas, and B. Akin, "Interturn short-circuit faults in permanent magnet synchronous machines: An extended review and comprehensive analysis," *IEEE Journal of Emerging and Selected Topics in Power Electronics*, vol. 6, no. 4, pp. 2173–2191, 2018.

[17] J. Faiz, H. Nejadi-Koti, and Z. Valipour, "Comprehensive review on inter-turn fault indexes in permanent magnet motors," *IET Electric Power Applications*, vol. 11, no. 1, pp. 142–156, 2017.

[18] P. F. C. Gonçalves, S. M. A. Cruz, and A. M. S. Mendes, "Open-phase fault diagnosis in six-phase pmsm drives based on the harmonics of the measured secondary subspace currents,"

in *IECON 2020 The 46th Annual Conference of the IEEE Industrial Electronics Society*, pp. 4863–4868, 2020.

[19] P. F. C. Gonçalves, S. M. A. Cruz, and A. M. S. Mendes, "Online diagnostic method for the detection of high-resistance connections and open-phase faults in six-phase pmsm drives," *IEEE Transactions on Industry Applications*, vol. 58, no. 1, pp. 345–355, 2022.

[20] Z. Ullah and J. Hur, "A comprehensive review of winding short circuit fault and irreversible demagnetization fault detection in pm type machines," *Energies*, vol. 11, no. 12, 2018.

[21] L. Vancini, M. Mengoni, G. Rizzoli, L. Zarri, and A. Tani, "Local demagnetization detection in six-phase permanent magnet synchronous machines," *IEEE Transactions on Industrial Electronics*, pp. 1–11, 2023.

[22] T. Ishikawa, Y. Seki, and N. Kurita, "Analysis for fault detection of vector-controlled permanent magnet synchronous motor with permanent magnet defect," *IEEE Transactions on Magnetics*, vol. 49, no. 5, pp. 2331–2334, 2013.

[23] C. Gao, B. Li, H. Chen, Y. Xu, X. Xu, J. Si, and Y. Hu, "A less-invasive method for accurately diagnosing demagnetization fault in pmsm using rotor partition," *IEEE Transactions on Transportation Electrification*, vol. 9, no. 2, pp. 2356–2366, 2023.

[24] J. A. Rosero, J. Cusido, A. Garcia, J. Ortega, and L. Romeral, "Broken bearings and eccentricity fault detection for a permanent magnet synchronous motor," in *IECON 2006 - 32nd Annual Conference on IEEE Industrial Electronics*, pp. 964–969, 2006.

[25] B. M. Ebrahimi, M. Javan Roshtkhari, J. Faiz, and S. V. Khatami, "Advanced eccentricity fault recognition in permanent magnet synchronous motors using stator current signature analysis," *IEEE Transactions on Industrial Electronics*, vol. 61, no. 4, pp. 2041–2052, 2014.

[26] Y. Chen, S. Liang, W. Li, H. Liang, and C. Wang, "Faults and diagnosis methods of permanent magnet synchronous motors: A review," *Applied Sciences*, vol. 9, p. 2116, 05 2019.

[27] F. L. T. Guefack, A. Kiselev, and A. Kuznietsov, "Improved detection of inter-turn short circuit faults in pmsm drives using principal component analysis," in *2018 International Symposium on Power Electronics, Electrical Drives, Automation and Motion (SPEEDAM)*, pp. 154–159, 2018.

[28] L. Romeral, J. C. Urresty, J.-R. Riba Ruiz, and A. Garcia Espinosa, "Modeling of surface-mounted permanent magnet synchronous motors with stator winding interturn faults," *IEEE Transactions on Industrial Electronics*, vol. 58, no. 5, pp. 1576–1585, 2011.

[29] J. A. Rosero, L. Romeral, J. A. Ortega, and E. Rosero, "Short-circuit detection by means of empirical mode decomposition and wigner–ville distribution for pmsm running under dynamic condition," *IEEE Transactions on Industrial Electronics*, vol. 56, no. 11, pp. 4534–4547, 2009.

[30] F. Alvarez-Gonzalez, A. Griffo, and B. Wang, "Permanent magnet synchronous machine stator windings fault detection by hilbert–huang transform," *The Journal of Engineering*, vol. 2019, no. 17, pp. 3505–3509, 2019.

[31] M. Kaminski, C. T. Kowalski, and T. Orlowska-Kowalska, "Application of radial basis neural networks for the rotor fault detection of the induction motor," in *2011 IEEE EUROCON - International Conference on Computer as a Tool*, pp. 1–4, 2011.

[32] S. Premrudeepreechacharn, T. Utthiyoung, K. Kruepengkul, and P. Puongkaew, "Induction motor fault detection and diagnosis using supervised and unsupervised neural networks," in *2002 IEEE International Conference on Industrial Technology, 2002. IEEE ICIT '02.*, vol. 1, pp. 93–96 vol.1, 2002.

[33] W. Lang, Y. Hu, C. Gong, X. Zhang, H. Xu, and J. Deng, "Artificial intelligence-based technique for fault detection and diagnosis of ev motors: A review," *IEEE Transactions on Transportation Electrification*, vol. 8, no. 1, pp. 384–406, 2022.

[34] J. Quiroga, L. Liu, and D. A. Cartes, "Fuzzy logic based fault detection of pmsm stator winding short under load fluctuation using negative sequence analysis," in *2008 American Control Conference*, pp. 4262–4267, 2008.

[35] M. A. Mazzoletti, G. R. Bossio, C. H. De Angelo, and D. R. Espinoza-Trejo, "A model-based strategy for interturn short-circuit fault diagnosis in pmsm," *IEEE Transactions on Industrial Electronics*, vol. 64, no. 9, pp. 7218–7228, 2017.

[36] F. Auger, M. Hilairet, J. M. Guerrero, E. Monmasson, T. Orlowska-Kowalska, and S. Katsura, "Industrial applications of the kalman filter: A review," *IEEE Transactions on Industrial Electronics*, vol. 60, no. 12, pp. 5458–5471, 2013.

[37] B. Aubert, J. Régnier, S. Caux, and D. Alejo, "Kalman-filter-based indicator for online interturn short circuits detection in permanent-magnet synchronous generators," *IEEE Transactions on Industrial Electronics*, vol. 62, no. 3, pp. 1921–1930, 2015.

[38] W. El Sayed, M. Abd El Geliel, and A. Lotfy, "Fault diagnosis of pmsg stator inter-turn fault using extended kalman filter and unscented kalman filter," *Energies*, vol. 13, no. 11, 2020.

[39] M. Hashemi, M. A. Golkani, and D. Watzenig, "A robust approach for inter-turn fault detection of pmsm used for autonomous vehicles," in *2022 International Conference on Connected Vehicle and Expo (ICCVE)*, pp. 1–6, 2022.

[40] A. Shawier, A. Habib, M. Mamdouh, A. S. Abdel-Khalik, and K. H. Ahmed, "Assessment of predictive current control of six-phase induction motor with different winding configurations," *IEEE Access*, vol. 9, pp. 81125–81138, 2021.

[41] Y. Zhao and T. Lipo, "Space vector pwm control of dual three-phase induction machine using vector space decomposition," *IEEE Transactions on Industry Applications*, vol. 31, no. 5, pp. 1100–1109, 1995.

[42] W.-H. Chen, "Disturbance observer based control for nonlinear systems," *IEEE/ASME Transactions on Mechatronics*, vol. 9, no. 4, pp. 706–710, 2004.

[43] W.-H. Chen, J. Yang, L. Guo, and S. Li, "Disturbance-observer-based control and related methods—an overview," *IEEE Transactions on Industrial Electronics*, vol. 63, no. 2, pp. 1083–1095, 2016.

[44] Y. Geng, P. Han, X. Chen, R. Chen, Z. Le, and Z. Lai, "On-line dead-time compensation method for dual three phase pmsm based on adaptive notch filter," *IET Power Electronics*, vol. 14, no. 15, pp. 2452–2465, 2021.

[45] X. Liu, W. Miao, Q. Xu, L. Cao, C. Liu, and P. W. T. Pong, "Inter-turn short-circuit fault detection approach for permanent magnet synchronous machines through stray magnetic field sensing," *IEEE Sensors Journal*, vol. 19, no. 18, pp. 7884–7895, 2019.

[46] C. Bianchini, E. Fornasiero, T. N. Matzen, N. Bianchi, and A. Bellini, "Fault detection of a five-phase permanent-magnet machine," in *2008 34th Annual Conference of IEEE Industrial Electronics*, pp. 1200–1205, 2008.

[47] Y. Gritli, M. Mengoni, C. Rossi, A. Tani, D. Casadei, and G. Serra, "Experimental assessment of winding inter-turn short-circuits fault signatures in six-phase ac permanent magnet

synchronous motors," *IET Renewable Power Generation*, vol. 14, no. 15, pp. 2791–2800, 2020.

[48] B. Wang, J. Wang, A. Griffo, and B. Sen, "Stator turn fault detection by second harmonic in instantaneous power for a triple-redundant fault-tolerant pm drive," *IEEE Transactions on Industrial Electronics*, vol. 65, no. 9, pp. 7279–7289, 2018.

[49] P. F. C. Gonçalves, S. M. A. Cruz, and A. M. S. Mendes, "Predictive current control of six-phase permanent magnet synchronous machines based on virtual vectors with optimal amplitude and phase," in *2019 International Conference on Smart Energy Systems and Technologies (SEST)*, pp. 1–6, 2019.

[50] S. M. A. Cruz, "An active–reactive power method for the diagnosis of rotor faults in three-phase induction motors operating under time-varying load conditions," *IEEE Transactions on Energy Conversion*, vol. 27, no. 1, pp. 71–84, 2012.

[51] P. F. Gonçalves, *Fault-Tolerant Predictive Control of PMSGs in Offshore Wind Turbines*. Ph.d thesis, Faculty of Sciences and Technology of the University of Coimbra, Coimbra, December 2021.

Appendix A

Six-phase PMSM Parameters

This appendix presents the six-phase PMSM parameters which were also used in the Ansys finite elements model. The six-phase PMSM drive parameters are provided in Table A.1.

Table A.1: Parameters of the six-phase PMSM.

Parameter	Value
Rated torque (T_n)	26.8 N.m
Rated current (I_n)	4.80 A
Power factor (FP)	1
Permanent magnet flux (ψ_{PM})	0.97 Wb
Rated frequency (f_n)	50 Hz
IEC frame size	132M
dq-axis inductance (L_{dq})	53.8 mH
xy-axis inductance (L_{xy})	2.1 mH
Number of pole pairs (p)	2
Rated power (P_n)	4 kW
Efficiency (η)	95%
Stator winding resistance (R_s)	1.55 Ω
Rated voltage (U_n)	340 V
Rated speed (n_m)	1500 rpm
Sampling period (T_s)	125 μs
Deadtime (T_d)	2.2 μs

Appendix B

Cosimulation Model Details

This appendix presents the six-phase PMSM Ansys simulation model interface.

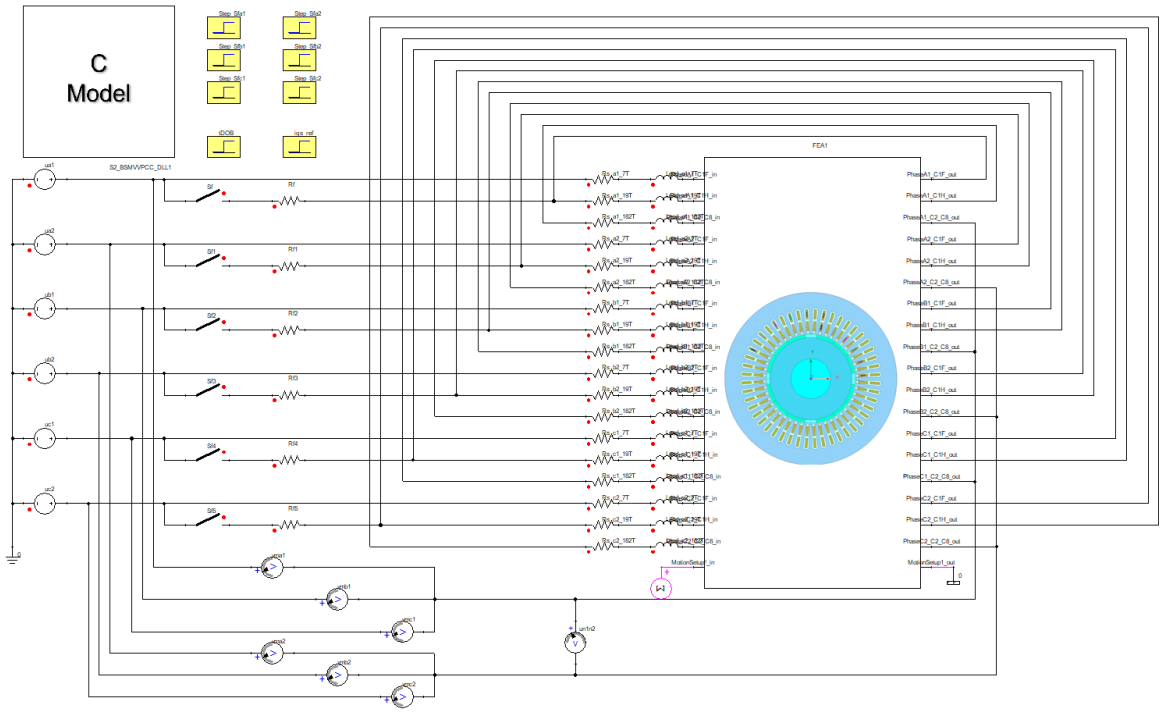

Figure B.1: Ansys simulation model interface.

Appendix C

Experimental Setup

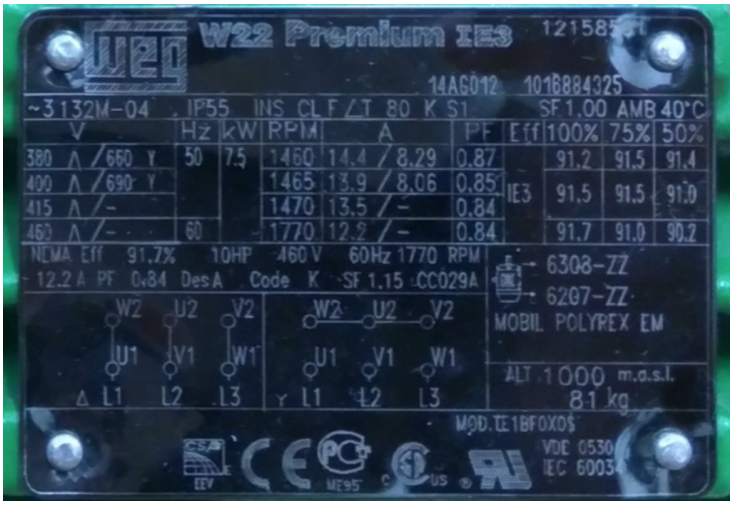

Figure C.1: Three-phase induction motor nameplate.

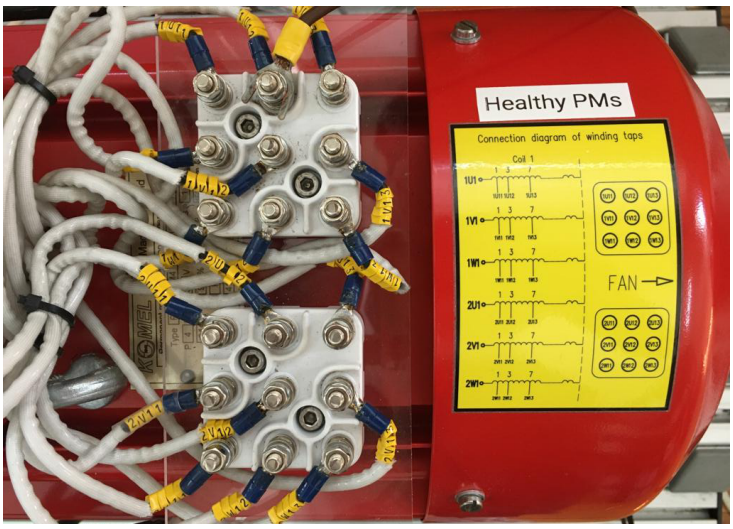

Figure C.2: Detail of the six-phase PMSM short-circuit connection terminals.

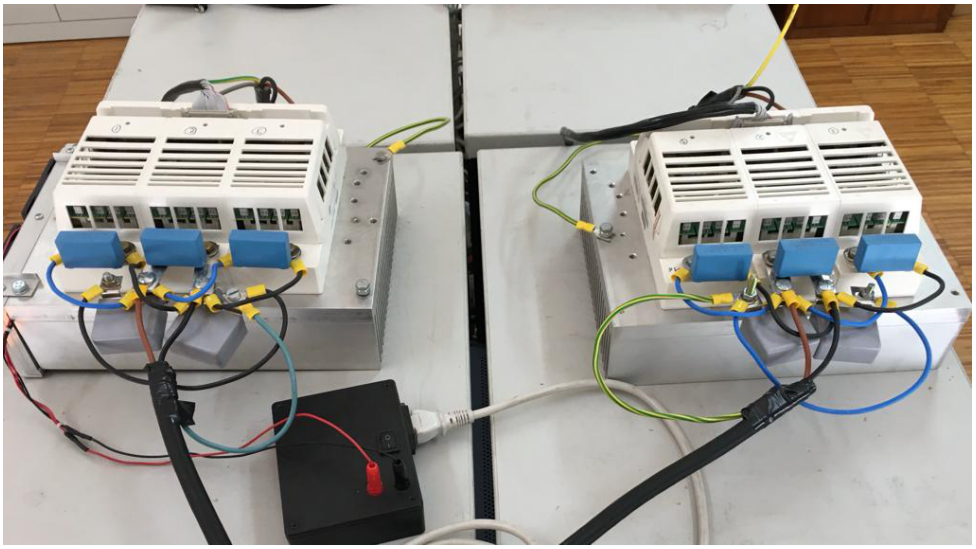

Figure C.3: 2L-VSIs used to power the six-phase PMSM.

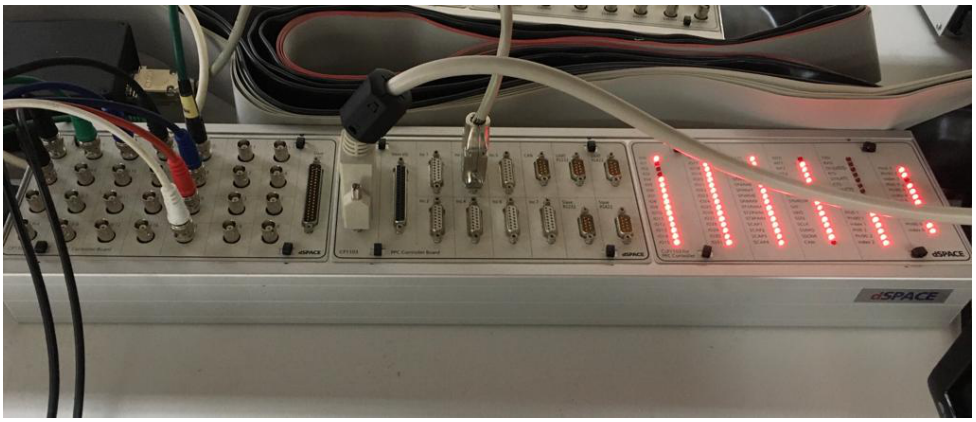

Figure C.4: dSPACE 1103 terminal panel.

Figure C.5: National Instruments cRIO-9066 controller.

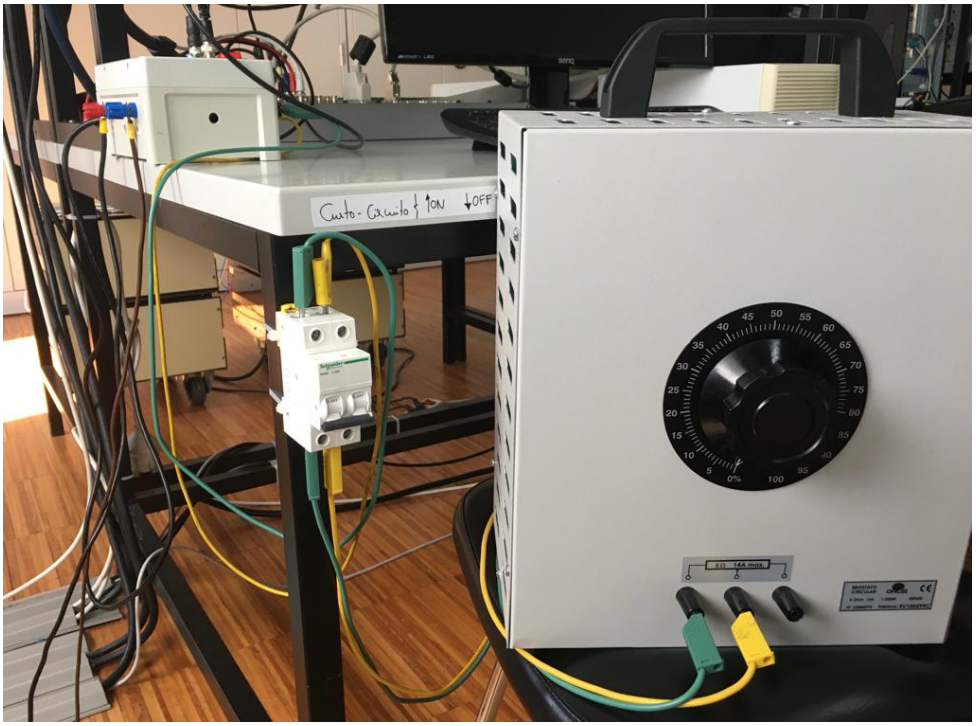

Figure C.6: Additional resistor used in the emulation of interturn short-circuits.

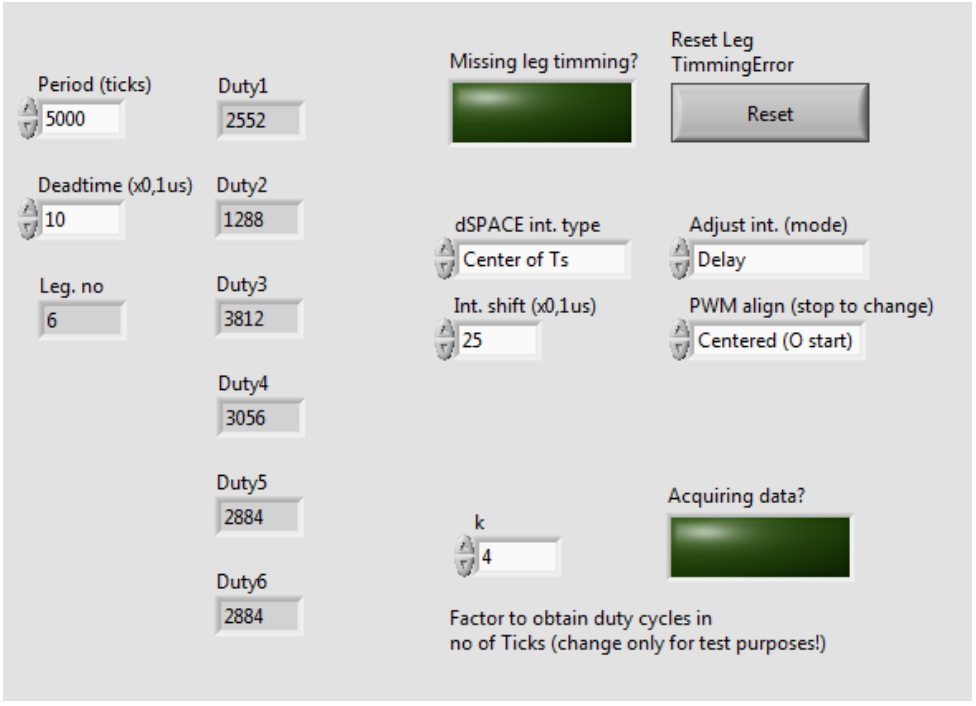

Figure C.7: Front panel built in LabVIEW to monitor and control the modulator running in the cRIO-9066.

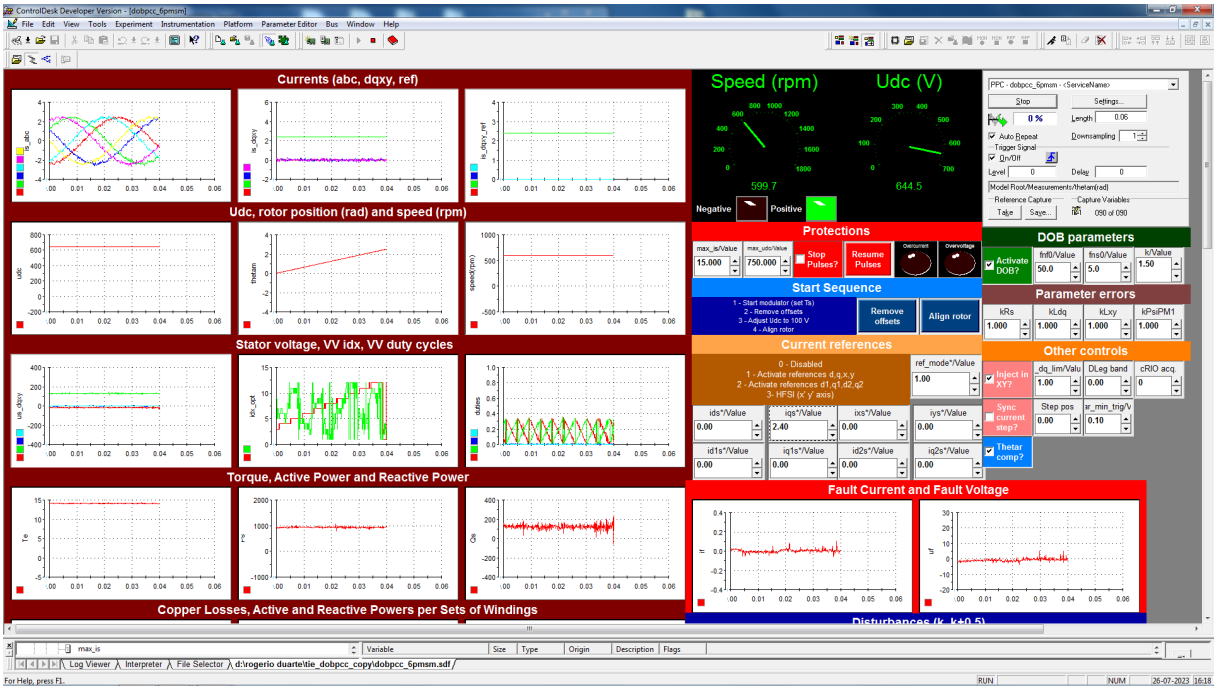

Figure C.8: Six-phase PMSM control panel built in ControlDesk.

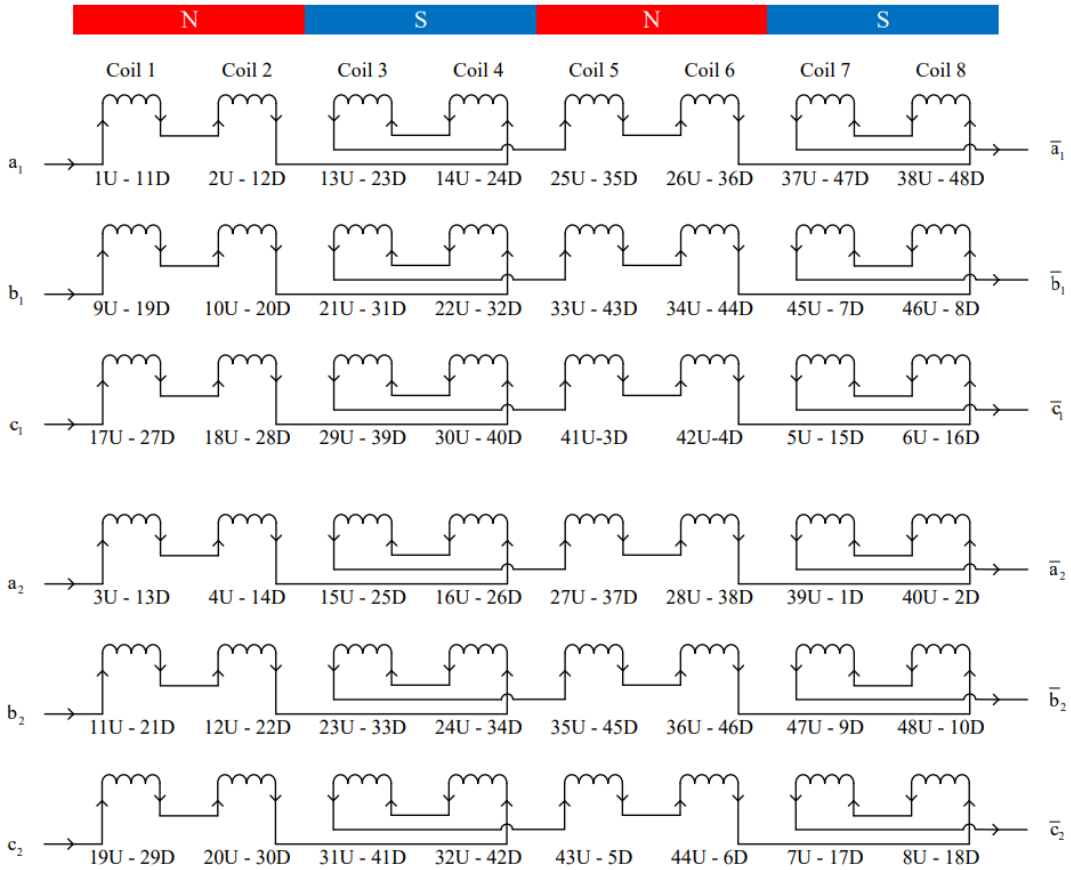

Figure C.9: Schematic of coil connections in each phase. Taken from [51]